Available online at www.sciencedirect.com
ScienceDirect
Comput. Methods Appl. Mech. Engrg. 372 (2020) 113307
Computer methods in applied mechanics and engineering
www.elsevier.com/locate/cma

Fractional topology optimization of periodic multi-material viscoelastic microstructures with tailored energy dissipation

Oliver Giraldo-Londoño, Glaucio H. Paulino*

School of Civil and Environmental Engineering, Georgia Institute of Technology, 790 Atlantic Drive, Atlanta, GA 30332, USA

Received 28 May 2019; received in revised form 17 July 2020; accepted 19 July 2020
Available online xxxx

Abstract

The microstructural configuration of a material affects its macroscopic viscoelastic behavior, which suggests that materials can be engineered to achieve a desired viscoelastic behavior over a range of frequencies. To this end, we leverage topology optimization to find the optimized topology of a multi-phase viscoelastic composite to tailor its energy dissipation behavior as a function of frequency. To characterize the behavior of each material phase, we use a fractional viscoelastic constitutive model. This type of material model uses differential operators of non-integer order, which are appropriate to represent hereditary phenomena with long- and short-term memory. The topology optimization formulation aims to find the lightest microstructure that minimizes the sum of squared loss modulus residuals for a given set of target frequencies. This leads to the design of materials with either maximized loss modulus for a given target frequency or tailored loss modulus for a predefined set of frequencies. We present several numerical examples, both in 2D and 3D, which demonstrate that the microstructural configuration of multi-phase materials affects its macroscopic viscoelastic behavior. Thus, if properly designed, the material behavior can be tailored to dissipate energy for a desired frequency (maximized loss modulus) or for a range of frequencies (tailored energy dissipation behavior).

Keywords: Topology optimization; Material design; Multi-phase composite; Fractional viscoelasticity; Fractional calculus; ZPR update scheme

1. Introduction

Materials with enhanced dissipative properties are attractive for applications involving control of noise and vibration of structures. For example, viscoelastic materials have traditionally been used for vibration damping of thin panels, such as those in automotive body structures, or those in the fuselage of an aircraft. In such structures, damping of vibration is commonly achieved via constrained-layer damping (CLD) treatments [1–3]. In a CLD treatment, a viscoelastic material is placed between two metallic sheets, creating a sandwich panel. When the panel vibrates, the viscoelastic material in its core deforms, dissipating energy into heat. The damping capabilities of a CLD treatment depend on both the layout of the damping layer and the viscoelastic properties of the material. In the present study, we focus on the latter, such that we design the microstructure of multi-phase viscoelastic composites with enhanced energy dissipation characteristics.

* Corresponding author.
E-mail address: paulino@gatech.edu (G.H. Paulino).

https://doi.org/10.1016/j.cma.2020.113307

Numerous studies have been conducted to find the optimal layout of CLD treatments in order to maximize the dissipation capabilities of a given structure. For instance, Zheng et al. [4] used a genetic algorithm to find the optimal distribution of rectangular viscoelastic patches in order to minimize a measure of the out-of-plane displacement of cylindrical shells subjected to transverse excitations. Alvelid [5] optimized the layout of a CLD treatment to minimize the frequency averaged transverse vibration levels of a plate subjected to harmonic excitations. In addition, Kang et al. [6] used topology optimization to find the distribution of a viscoelastic material on the surface of a thin-shell structure in order to minimize the amplitude of vibration at a given location. Topology optimization was also used by Kim et al. [7] and by Yamamoto et al. [8] to find the layout of a damping treatment maximizing the modal loss factor of shell structures. Similar objectives were pursued by Moreira and Dias Rodrigues [9] and by Ling et al. [10].

Despite the umpteen number of investigations dedicated to finding the optimal layout of CLD treatments, studies aiming to optimize optimizing the viscoelastic properties of the material are more scarce. The microstructural configuration of a material (i.e., the topological distribution of material inside a unit cell) affects its macroscopic viscoelastic behavior [11]. This observation was used by Yi et al. [12] to design the microstructure of viscoelastic composites using topology optimization. The objective of their work was to design microstructures with enhanced damping characteristics for a particular design frequency. Their problem was setup as an inverse homogenization problem, similar to that proposed by Sigmund [13,14] for the design of elastic materials. More recently, Andreassen and Jensen [15] presented a topology optimization formulation for the design of material microstructures that maximize attenuation of propagating waves. The microstructures obtained in their work were made of two material phases: a stiff, non-dissipative phase, and a compliant, dissipative phase (i.e., no void is present in the optimized microstructures).

Andreasen et al. [16] presented a methodology for the design of two-phase viscoelastic microstructures, both in 2D and 3D, maximizing the imaginary part of the complex bulk modulus (i.e., the bulk loss modulus). They showed that the microstructures obtained using their formulation are able to reach theoretical upper bounds for the bulk loss modulus by Gibiansky and Lakes [17,18]. Another methodology for the design of viscoelastic microstructures was presented by Chen and Liu [19]. In their study, the authors aimed to minimize the square difference between the homogenized shear modulus of the viscoelastic composite and a target value, while considering only one viscoelastic material phase and void.

Using the bi-directional evolutionary structural optimization (BESO) method, Huang et al. [20] presented a methodology for the design of microstructures made of viscoelastic materials. The microstructures obtained in their study were made of two materials, in which one was stiff and elastic and the other was compliant and viscoelastic. Huang et al. [20] defined an artificial two-phase material that uses the solid isotropic material penalization (SIMP) method to interpolate between the storage modulus tensors of the two materials and uses linear interpolation to interpolate between the loss modulus tensors of the two materials. The authors considered two objective functions, the first being the homogenized loss tangent of the composite and the second its homogenized storage modulus. The authors found that, when maximizing the storage modulus of the composite, they were able to achieve the lower bound of the effective bulk modulus in the complex plane, and when maximizing for damping, they were able to achieve the upper bound.

Recently, Andreassen and Jensen [21] presented a multi-scale approach for maximizing structural damping. In their approach, a series of isotropic microstructures with maximized loss factor were first obtained. These microstructures were designed such that they can all be connected through a stiff phase, which facilitates the manufacturability of the macrostructure using additive manufacturing. They used the homogenized properties of the microstructures to determine a material interpolation function that can be used for the design of the macrostructure. Then, they maximized the damping of the macrostructure and used the optimized microstructures based on the given optimal density obtained from the topology optimization of the macrostructure. Another multiscale approach was presented by Chen and Liu [22] for the design of CLD treatments maximizing the modal loss factor of the macrostructure. The modal loss factor of the macrostructure was obtained via the modal strain energy method. The viscoelastic layer is assumed homogeneous and composed of periodic unit cells repeated in space. Their results showed that the use of cellular viscoelastic materials can be more advantageous than the use of solid viscoelastic materials in order to damp vibrations.

Asadpoure et al. [23] presented a methodology for the design of multi-phase viscoelastic microstructures composed of two material phases and void. One of the material phases is stiff and elastic, while the other is compliant

and viscoelastic. The objective of their topology optimization formulation was to obtain the distribution of material within a unit cell in order to maximize both the lowest natural frequency and the intrinsic damping characteristics of a macrostructure. To that end, they proposed an objective function of the form $E^{1/3}\tan\delta/\rho$, where E, ρ, and $\tan\delta$ are the Young's modulus, density, and damping coefficient of the material, respectively. To determine the damping coefficient, they considered inertial effects by means of the Bloch–Floquet theorem. In addition, to obtain effective viscoelastic properties for intermediate element densities, Asadpoure et al. [23] used an interpolation scheme for a three-phase composite that was adopted from the interpolation scheme introduced by Sigmund and Torquato [24]. Similar to observations by Chen and Liu [22], the results by Asadpoure et al. [23] indicated that the performance of optimized cellular materials surpasses that of dense materials.

The studies above have focused on the design of viscoelastic composites made of two materials, in which one is typically stiff and elastic and the other is soft and viscoelastic. Commonly used viscoelastic materials can damp vibration efficiently on a narrow range of frequencies and temperatures [25]. As a result, multi-phase materials designed with a single viscoelastic phase are likely to damp vibrations efficiently only for a narrow range of frequencies and temperatures. This type of restriction is not desired in CLD treatments, for instance in applications involving aircraft and terrestrial vehicles, because of the large temperature changes that these structures suffer during operation, which may affect their dynamic performance significantly.

The goal of this work is to introduce a methodology for the design of multi-material viscoelastic microstructures whose dissipative properties can be tailored over a predefined range of frequencies. To tailor the viscoelastic response of the material, we minimize the sum of squared loss modulus residuals, where the residual for each frequency is computed as the difference between the homogenized loss modulus and a target loss modulus. In addition to minimizing the sum of squared residuals, we also minimize the volume of the structure, which allows us design microstructures with less amount of material. The formulation uses a general volume constraint setting, so that constraints can be imposed to a subset of the candidate materials, to sub-regions of the design domain, or to a combination of both. To compute the effective viscoelastic properties for intermediate element densities, we adopt the Discrete Material Optimization (DMO) interpolation scheme [26,27], which has successfully been used for the topology optimization of layered materials as well as for the design of multi-material structures in the context of density-based topology optimization [28]. To model the behavior of each material phase, we use a fractional viscoelastic constitutive model, which uses differential operators of non-integer order that can represent hereditary phenomena with long- and short-term memory, such as that observed in soft materials (polymers, tissues, etc.). We use the proposed approach to design 2D and 3D multi-phase materials with various energy dissipation characteristics (e.g., high damping for low frequencies, high damping for high frequencies, or plateau-type damping for a wide range of frequencies).

The remainder of this paper is organized as follows. Section 2 discusses concepts on homogenization theory for viscoelastic materials in frequency domain. In Section 3, we detail the topology optimization formulation for the design of multi-material viscoelastic microstructures, followed by the description of the design variable update scheme in Section 4. We add a few implementation details in Section 5 and present several numerical examples in Section 6. In Section 7, we discuss the computational efficiency of the present approach, with emphasis on the efficiency of the design variable update scheme. We finalize the paper with some concluding remarks in Section 8. Afterwards, we present an Appendix with verification of the numerical homogenization of the complex modulus tensor based on mutual energies.

2. Homogenization of linearly viscoelastic materials in the frequency domain

In this section, we summarize relevant concepts related to the homogenization of viscoelastic materials in the frequency domain. Consider a uniform viscoelastic material subjected to a harmonic excitation with frequency ω. The steady-state stress–strain response of this material, assuming isothermal conditions, is also harmonic and can be represented as follows:

$$\bar{\boldsymbol{\sigma}}(\omega) = \mathbf{E}^*(\omega)\bar{\boldsymbol{\varepsilon}}(\omega), \tag{1}$$

where $\bar{\boldsymbol{\sigma}}(\omega)$ and $\bar{\boldsymbol{\varepsilon}}(\omega)$ are the Fourier transforms of the stress and strain tensors, respectively. The complex modulus tensor, $\mathbf{E}^*(\omega)$, can be separated into its real and imaginary parts, as

$$\mathbf{E}^*(\omega) = \mathbf{E}'(\omega) + i\mathbf{E}''(\omega), \tag{2}$$

where $\mathbf{E}'(\omega)$ and $\mathbf{E}''(\omega)$ are the storage and loss moduli tensors, respectively.

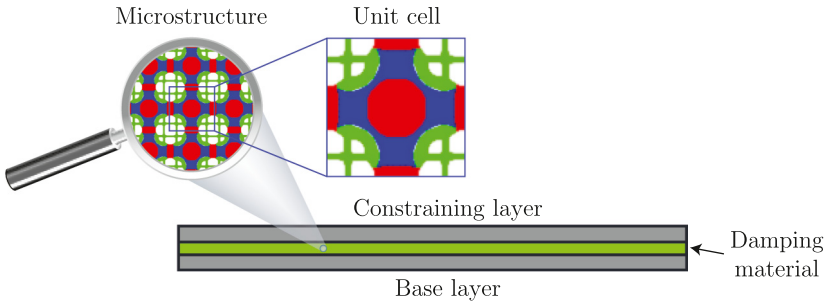

Fig. 1. Viscoelastic material used as passive energy dissipation mechanism in a constrained-layer damping treatment. At the microscopic scale, we assume a periodic microstructure composed of multiple material phases.

Now, consider a macroscopic structure made of a viscoelastic cellular material such as that shown in Fig. 1. In the cellular material of Fig. 1, we assume that the microstructure is composed of unit cells that are periodically repeated in space. If we further assume that the size of the unit cell is small enough in comparison with the wavelength of the waves propagating through the macrostructure, one can homogenize the response of the material over the unit cell [20]. The homogenized response of the material in the frequency domain is similar to that shown in Eq. (1), but it is given in terms of the homogenized (or effective) complex modulus tensor, $\mathbf{E}^{*H}(\omega)$, as follows:

$$\bar{\boldsymbol{\sigma}}(\omega) = \mathbf{E}^{*H}(\omega)\bar{\boldsymbol{\varepsilon}}(\omega). \tag{3}$$

The homogenized complex modulus tensor depends on the properties of the materials that compose the unit cell, their volume fraction, and their spatial distribution [11,12,20].

Using asymptotic expansions [11,12,20], we obtain the homogenized complex modulus tensor (in indicial notation):

$$E^{*H}_{ijkl}(\omega) = \frac{1}{|Y|}\int_Y E^*_{ijpq}(\mathbf{y},\omega)\left(\bar{\varepsilon}^{(kl)}_{pq} - \tilde{\varepsilon}^{(kl)}_{pq}\right)\mathrm{d}Y, \tag{4}$$

where $\mathbf{E}^*(\mathbf{y},\omega)$ is the space- and frequency-dependent complex modulus tensor at each point $\mathbf{y}$ inside the unit cell, and $Y = (0,\ Y_1)\times(0,\ Y_2) \in \mathbb{R}^2$ (or $Y = (0,\ Y_1)\times(0,\ Y_2)\times(0,\ Y_3) \in \mathbb{R}^3$) is the 2D (or 3D) domain defining the unit cell. The unit test strain fields, $\bar{\varepsilon}^{(kl)}_{pq}$, are applied at the boundaries of the unit cell [13], and the strain fields, $\tilde{\varepsilon}^{(kl)}_{pq}$, induced by the unit test strains, $\bar{\varepsilon}^{(kl)}_{pq}$, are obtained as the Y-periodic solution of the boundary value problem [12]:

$$\begin{aligned}&\int_Y E^*_{ijpq}(\mathbf{y},\omega)\tilde{\varepsilon}^{(kl)}_{pq}\frac{\partial v_i}{\partial y_j}\mathrm{d}Y = \int_Y E^*_{ijpq}(\mathbf{y},\omega)\bar{\varepsilon}^{(kl)}_{pq}\frac{\partial v_i}{\partial y_j}\mathrm{d}Y,\\ &\quad \forall \mathbf{v} \in V_Y = \{\mathbf{v}|v_i \in H^1_{loc}(\mathbb{R}^d),\ Y-\text{periodic}\},\end{aligned} \tag{5}$$

where $d = 2$ for 2D unit cells and $d = 3$ for 3D unit cells. The homogenized complex modulus tensor is obtained by first solving the periodic boundary value problem (5) and then using Eq. (4). Because the boundary value problem (5) is defined in terms of the complex modulus tensor $\mathbf{E}^*(\mathbf{y},\omega)$, its solution requires the use of complex stiffness matrices for each finite element [12,19].

3. Multi-material topology optimization formulation

We present a topology optimization approach to tailor the macroscopic damping characteristics of a cellular viscoelastic composite as a function of frequency. The viscoelastic composite can be composed of up to m candidate materials, each with a different viscoelastic behavior. The topology optimization statement is designed to find the least amount of material that minimizes the sum of squared loss modulus residuals for a given set of target frequencies. We define the residual at a particular frequency as the difference between the homogenized loss modulus and a target loss modulus at that frequency. The topology optimization problem is stated mathematically as follows:

$$
\begin{aligned}
\min_{\mathbf{z}_1,\ldots,\mathbf{z}_m} \quad & J(\mathbf{z}_1,\ldots,\mathbf{z}_m) = \bar{r}(\mathbf{z}_1,\ldots,\mathbf{z}_m,\omega_1,\ldots,\omega_N) + \xi\bar{m}(\mathbf{z}_1,\ldots,\mathbf{z}_m) \\
\text{s.t.} \quad & g_j = \frac{\sum_{i\in\mathcal{M}_j}\sum_{e\in\mathcal{E}_j} v_e\rho_i^e}{\sum_{e\in\mathcal{E}_j} v_e} - \bar{v}_j \le 0, \quad j = 1,\ldots,N_c \\
& 0 < z_{\min} \le z_i^e \le 1, \quad e = 1,\ldots,N_e, \quad i = 1,\ldots,m \\
\text{with:} \quad & \int_Y E^*_{ijpq}(\mathbf{y},\omega)\tilde{\varepsilon}^{kl}_{pq}\frac{\partial v_i}{\partial y_j}\mathrm{d}Y = \int_Y E^*_{ijpq}(\mathbf{y},\omega)\bar{\varepsilon}^{kl}_{pq}\frac{\partial v_i}{\partial y_j}\mathrm{d}Y, \quad \forall\mathbf{v}\in V_Y \\
& E^{*H}_{ijkl}(\omega) = \frac{1}{|Y|}\int_Y E^*_{ijpq}(\mathbf{y},\omega)(\bar{\varepsilon}^{kl}_{pq} - \tilde{\varepsilon}^{kl}_{pq})\mathrm{d}Y, \\
& \tilde{\rho}_i^e = \frac{\tanh(\beta\eta) + \tanh(\beta(\rho_i^e - \eta))}{\tanh(\beta\eta) + \tanh(\beta(1-\eta))}, \quad e = 1,\ldots,N_e, \quad i = 1,\ldots,m, \\
& \boldsymbol{\rho}_i = \mathbf{P}\mathbf{z}_i, \quad i = 1,\ldots,m.
\end{aligned}
\tag{6}
$$

The first term of the objective function, $\bar{r}$, corresponds to the sum of squared loss modulus residuals normalized with respect to the initial sum of squared loss modulus residuals, which we compute as

$$
\bar{r}(\mathbf{z}_1,\ldots,\mathbf{z}_m,\omega_1,\ldots,\omega_N) = \frac{1}{r_0}\sum_{i=1}^{N}\left[E''_H(\mathbf{z}_1,\ldots,\mathbf{z}_m,\omega_i) - E''(\omega_i)\right]^2, \tag{7}
$$

where r_0 is the initial sum of squared loss modulus residuals (i.e., computed for the initial density distribution); $E''(\omega_i)$ is the target loss modulus at target frequency, ω_i; $E''_H(\mathbf{z}_1,\ldots,\mathbf{z}_m,\omega_i)$ is the homogenized loss modulus at target frequency, ω_i; and N is the number of target points. We approximately compute the homogenized loss modulus as

$$
E''_H = \frac{1}{2}(E''^H_{1111} + E''^H_{2222}) \tag{8}
$$

for 2D microstructures and

$$
E''_H = \frac{1}{3}(E''^H_{1111} + E''^H_{2222} + + E''^H_{3333}) \tag{9}
$$

for 3D microstructures, where the terms E''^H_{ijkl} are components of the homogenized loss modulus tensor, which are obtained from $(6)_5$. The second term of the objective function, $\bar{m}$, corresponds to the mass (volume) of the unit cell normalized with respect to the mass computed for the initial density distribution. That is,

$$
\bar{m}(\mathbf{z}_1,\ldots,\mathbf{z}_m) = \frac{1}{m_0}\sum_{i=1}^{m}\sum_{e=1}^{N_e} v_e[\tilde{\rho}_i^e + \delta\tilde{\rho}_i^e(1-\tilde{\rho}_i^e)], \tag{10}
$$

where m_0 is the mass computed for the initial density distribution. We have added additional terms $\delta\tilde{\rho}_i^e(1-\tilde{\rho}_i^e)$ to (10) to help drive the design variables toward 0 or 1. Finally, parameter $\xi > 0$ in (6) is a scalar weight factor, which we add to control the relative importance between the mass term and the residual term.

In the optimization statement (6), the design variables, $\mathbf{z}_1,\ldots,\mathbf{z}_m$, are vectors of element densities (one for each of the m candidate materials); $\mathbf{E}^*_H$ is the homogenized complex modulus tensor; g_j, $j = 1,\ldots,N_c$ is the jth volume constraint, which can be imposed to a subset of the candidate materials, to sub-regions of the unit cell, or to a combination of both [28,29]; $\mathcal{M}_j$ is the set of material indices associated with volume constraint j; $\mathcal{E}_j$ is the set of element indices associated with volume constraint j; v_e is the volume (or area) of finite element e; ρ_i^e is the filtered density of finite element e associated with candidate material i; $\bar{v}_j$ is the volume fraction limit associated with constraint j; N_c is the total number of volume constraints; and N_e is the total number of elements in the finite element mesh.

The vector of filtered densities for each candidate material is obtained as $\boldsymbol{\rho}_i = \mathbf{P}\mathbf{z}_i$, $i = 1,\ldots,m$, where $\mathbf{P}$ is the filter matrix. In this study, we use a nonlinear filter, such that components of the filter matrix are obtained as [30]:

$$
P_{ij} = \frac{w_{ij}v_j}{\sum_{k=1}^{N_e} w_{ik}v_k}, \quad \text{with} \quad w_{ij} = \max\left(0,\ 1 - \frac{\|\mathbf{x}_i - \mathbf{x}_j\|_2}{R}\right)^q. \tag{11}
$$

The term $\|\mathbf{x}_i - \mathbf{x}_j\|_2$ in Eq. (11)$_2$ refers to the distance between the centroids $\mathbf{x}_i$ and $\mathbf{x}_j$ of elements i and j, respectively, R is the prescribed filter radius, and q is the nonlinear filter exponent. The nonlinear filter shown above reduces to a traditional linear filter [31] when $q = 1$. Note that there is only one filter matrix, which is independent of the number of candidate materials, m.

3.1. Material interpolation scheme

The topology optimization statement introduced previously considers m candidate materials. Therefore, it is necessary to choose an appropriate material interpolation scheme that can handle multiple materials. Typical topology optimization formulations for viscoelastic material design have been limited to two candidate materials, for which a SIMP-like, or a linear interpolation scheme, with one design variable per element, suffices (e.g., see [15,16,20]). Because our topology optimization formulation allows for m candidate materials (with $m \geq 2$), we consider multiple design variables per element. In this work, we use a material interpolation scheme that is adopted from studies on density-based topology optimization for elastic multi-material (or multi-layered) structures. Specifically, we use the Discrete Material Optimization (DMO) parametrization [26,27]. The DMO formulation is an extension of the Solid Isotropic Material with Penalization (SIMP) interpolation scheme [32,33], which considers m candidate materials, leading to 0/1 designs at the end of the optimization steps.

The DMO parametrization was designed for linear elastic materials, in particular for the design of composite shell structures [26,27]. The DMO interpolation was used in a study by Sanders et al. [34], which focused on the compliance minimization of multi-material structures using density-based topology optimization. In the traditional DMO interpolation, the element elasticity tensor, $\mathbf{E}_e$, is expressed as

$$\mathbf{E}_e(\rho_1^e, \ldots, \rho_m^e) = \sum_{i=1}^{m} w_i \mathbf{E}_i, \quad \text{with} \quad w_i = (\tilde{\rho}_i^e)^p \prod_{\substack{j=1 \\ j \neq i}}^{m} \left[1 - (\tilde{\rho}_j^e)^p\right], \tag{12}$$

where w_i are weight factors [26,27][1] and $\mathbf{E}_i$ is the elasticity tensor for solid candidate material i.

The penalty parameter, p, in Eq. (12)$_2$ is similar to that used in the SIMP interpolation scheme, and the product term is used to push the design variables toward 0 and 1. In this study, we use the modified DMO interpolation scheme introduced by Sanders et al. [34] and apply it to both the real and the imaginary parts of the complex modulus tensor, as follows:

$$\begin{aligned} E_e'(\rho_1^e, \ldots, \rho_m^e, \omega) &= \varepsilon + (1 - \varepsilon) \sum_{i=1}^{m} w_i^R E_i'^0(\omega) \quad \text{and} \\ E_e''(\rho_1^e, \ldots, \rho_m^e, \omega) &= \varepsilon + (1 - \varepsilon) \sum_{i=1}^{m} w_i^I E_i''^0(\omega), \end{aligned} \tag{13}$$

where

$$w_i^R = (\tilde{\rho}_i^e)^{p_R} \prod_{\substack{j=1 \\ j \neq i}}^{m} \left[1 - \gamma(\tilde{\rho}_j^e)^{p_R}\right] \quad \text{and} \quad w_i^I = (\tilde{\rho}_i^e)^{p_I} \prod_{\substack{j=1 \\ j \neq i}}^{m} \left[1 - \gamma(\tilde{\rho}_j^e)^{p_I}\right] \tag{14}$$

are the weight functions used for the storage modulus and the loss modulus, respectively. The term ε is an Ersatz-like parameter used to prevent the stiffness matrices from becoming singular and the terms $E_i'^0(\omega)$ and $E_i''^0(\omega)$ correspond to the storage and loss modulus of solid material i, $i = 1, \ldots, m$, respectively, evaluated at frequency ω. The penalty parameters p_R and p_I are used to penalize the storage and loss modulus, respectively. Parameter γ ($0 \leq \gamma \leq 1$) controls the amount of penalization due to material mixing. For instance, from Eq. (14), $\gamma = 1$ leads to $w_i^R = 0$ and $w_i^I = 0$ when material mixing is present (i.e., full penalization of material mixing), whereas $\gamma = 0$ leads to $w_i^R = 1$ and $w_i^I = 1$ when material mixing is present (i.e., no penalization of material mixing). In order to achieve better optimization results, we use a continuation scheme in parameters γ, p_R, and p_I, in a similar way as conducted by Sanders et al. [34].

[1] Another choice of weight factors used by Stegmann and Lund [26] and Lund and Stegmann [27] is $w_i = (\tilde{\rho}_i^e)^p$; however, this type of weight function fails to push the design variables toward 0 and 1 and leads to a considerable amount of material mixing at the end of the optimization iterations.

3.2. Sensitivity analysis

We solve the topology optimization problem (6) using gradient-based optimization methods. Therefore, we need to obtain the sensitivity of the objective function and constraints with respect to the design variables. To obtain the sensitivity of the objective function, we first rewrite Eq. (4) in terms of mutual energies [13]:

$$E^{*H}_{ijkl}(\omega) = \frac{1}{|Y|}\int_Y E^*_{pqrs}(\mathbf{y},\omega)\left(\bar{\varepsilon}^{(kl)}_{pq} - \tilde{\varepsilon}^{(kl)}_{pq}\right)\left(\bar{\varepsilon}^{(ij)}_{rs} - \tilde{\varepsilon}^{(ij)}_{rs}\right)\mathrm{d}Y. \tag{15}$$

Now, we differentiate Eq. (15), with respect to $\tilde{\rho}^e_a$, leading to

$$\begin{aligned}\frac{\partial E^{*H}_{ijkl}(\omega)}{\partial \tilde{\rho}^e_a} =& \frac{1}{|Y|}\int_Y \frac{\partial E^*_{pqrs}(\mathbf{y},\omega)}{\partial \tilde{\rho}^e_a}\left(\bar{\varepsilon}^{(kl)}_{pq} - \tilde{\varepsilon}^{(kl)}_{pq}\right)\left(\bar{\varepsilon}^{(ij)}_{rs} - \tilde{\varepsilon}^{(ij)}_{rs}\right)\mathrm{d}Y \\ &- \frac{1}{|Y|}\int_Y E^*_{pqrs}(\mathbf{y},\omega)\frac{\partial \tilde{\varepsilon}^{(kl)}_{pq}}{\partial \tilde{\rho}^e_a}\left(\bar{\varepsilon}^{(ij)}_{rs} - \tilde{\varepsilon}^{(ij)}_{rs}\right)\mathrm{d}Y \\ &- \frac{1}{|Y|}\int_Y E^*_{pqrs}(\mathbf{y},\omega)\frac{\partial \tilde{\varepsilon}^{(ij)}_{rs}}{\partial \tilde{\rho}^e_a}\left(\bar{\varepsilon}^{(kl)}_{pq} - \tilde{\varepsilon}^{(kl)}_{pq}\right)\mathrm{d}Y.\end{aligned} \tag{16}$$

Following a similar procedure as that by Yi et al. [12], we expand the second term on the right-hand side of Eq. (16) as follows:

$$\begin{aligned}\frac{1}{|Y|}\int_Y E^*_{pqrs}(\mathbf{y},\omega)\frac{\partial \tilde{\varepsilon}^{(kl)}_{pq}}{\partial \tilde{\rho}^e_a}\left(\bar{\varepsilon}^{(ij)}_{rs} - \tilde{\varepsilon}^{(ij)}_{rs}\right)\mathrm{d}Y =& \frac{1}{|Y|}\int_Y E^*_{pqrs}(\mathbf{y},\omega)\bar{\varepsilon}^{(ij)}_{rs}\frac{\partial \tilde{\varepsilon}^{(kl)}_{pq}}{\partial \tilde{\rho}^e_a}\mathrm{d}Y \\ &- \frac{1}{|Y|}\int_Y E^*_{pqrs}(\mathbf{y},\omega)\tilde{\varepsilon}^{(ij)}_{rs}\frac{\partial \tilde{\varepsilon}^{(kl)}_{pq}}{\partial \tilde{\rho}^e_a}\mathrm{d}Y.\end{aligned} \tag{17}$$

Because the solution of Eq. (5) is Y-periodic independently of the density distribution, then $\partial\tilde{\varepsilon}^{(kl)}_{pq}/\partial\tilde{\rho}^e_a \in V_Y = \{\mathbf{v}|v_i \in H^1_{loc}(\mathbb{R}^d),\ Y-\text{periodic}\}$, in which $d = 2$ for 2D microstructures and $d = 3$ for 3D microstructures. In addition, because (5) is valid for any function $\mathbf{v} \in V_Y$, then the two terms on the right hand side of (17) are equal, and thus, (17) becomes zero. Likewise, the third term on the right-hand side of (16) becomes zero, which leads to the following expression for the sensitivity of the homogenized complex modulus tensor:

$$\frac{\partial E^{*H}_{ijkl}(\omega)}{\partial \tilde{\rho}^e_a} = \frac{1}{|Y|}\int_Y \frac{\partial E^*_{pqrs}(\mathbf{y},\omega)}{\partial \tilde{\rho}^e_a}\left(\bar{\varepsilon}^{(kl)}_{pq} - \tilde{\varepsilon}^{(kl)}_{pq}\right)\left(\bar{\varepsilon}^{(ij)}_{rs} - \tilde{\varepsilon}^{(ij)}_{rs}\right)\mathrm{d}Y. \tag{18}$$

The sensitivity of the homogenized complex modulus with respect to the design variables, ρ^e_a, is obtained by the chain rule and Eq. (18), as follows:

$$\frac{\partial E^{*H}_{ijkl}(\omega)}{\partial \rho^e_a} = \frac{\partial E^{*H}_{ijkl}(\omega)}{\partial \tilde{\rho}^e_b}\frac{\partial \tilde{\rho}^e_b}{\partial \rho^e_a}. \tag{19}$$

The sensitivity of the homogenized complex modulus tensor can be used to obtain the sensitivity of the objective function in (6) via the chain rule.

3.3. Fractional material model

Most studies related to design of microstructures made of viscoelastic materials consider simple viscoelastic material models with relaxation functions of the form $E(t) = a + be^{-t/\tau}$, in which a, b, and τ are material constants. This type of material model, which is representative of a standard linear solid model or a Zener model, is often insufficient to represent the behavior of real viscoelastic materials, such as polymers, which are often used in additive manufacturing [35–37]. Given that current additive manufacturing technologies allow manufacturing of these types of microstructures [38–41], it is critical that we model the viscoelastic behavior of polymers accurately in our formulation.

Simulating the actual viscoelastic behavior of polymers requires the use of an adequate material model, and this study accomplishes it by means of a fractional viscoelastic model. Fractional viscoelastic models have proven adequate to represent the behavior of several materials, including polymers [42,43], bituminous materials [44], and

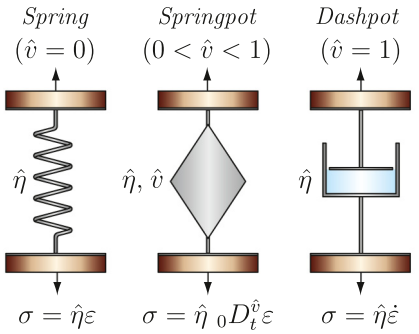

Fig. 2. A springpot (center) is an element with physical behavior between that of a spring (left) and that of a dashpot (right), and it represents a spring when $\hat{v} \to 0$ and a dashpot when $\hat{v} \to 1$.

biological tissue [45–47]. In fractional viscoelastic models, fractional calculus[2] is used to write the constitutive relation of the material in terms of differential operators of non-integer order [51]. An example of a fractional differential operator used in fractional viscoelasticity is the *Caputo fractional derivative* of order $\hat{v} \in (0,\ 1)$,

$$ {}_0D_t^{\hat{v}} f(t) = \frac{1}{\Gamma(1-\hat{v})} \int_0^t \frac{\dot{f}(\tau)}{(t-\tau)^{\hat{v}}} \mathrm{d}\tau, \tag{20} $$

where $\Gamma(\cdot)$ is the Gamma function, and the left and right subscripts in ${}_0D_t^{\hat{v}}$ refer to the lower and upper limits of the integral in (20).

A Caputo fractional derivative of order $\hat{v} \in (0,\ 1)$ can be used to represent the stress–strain behavior of a viscoelastic material with power-law type stress relaxation function, $E(t) \sim t^{-\hat{v}}$, as follows:

$$ \sigma(t) = \hat{\eta}\ {}_0D_t^{\hat{v}}\varepsilon(t) = \frac{\hat{\eta}}{\Gamma(1-\hat{v})} \int_0^t \frac{\dot{\varepsilon}(\tau)}{(t-\tau)^{\hat{v}}} \mathrm{d}\tau, \tag{21} $$

where $\hat{\eta}$ is a stiffness-like parameter. The constitutive relationship (21) was proposed by Scott-Blair [52] to describe a material that behaves between a Hookean solid and a Newtonian fluid. Because of this characteristic behavior, a material whose behavior is governed by Eq. (21) is referred to as a *springpot*. From (21), one can infer that a springpot becomes a linear spring when $\hat{v} \to 0$ and becomes a dashpot when $\hat{v} \to 1$. These two limit behaviors are illustrated in Fig. 2, in which the springpot is depicted as a diamond-shaped element.

The three elements shown in Fig. 2 can be used to generate rheological models of fractional order. One of the simplest rheological models of fractional order is the fractional standard linear solid (SLS) model [51]. This model, which is defined in terms of four parameters, is shown in Fig. 3. Parameters $\hat{\eta}$ and $\hat{v}$ define the behavior of the springpot (diamond-shaped element), and parameters E and c define the behavior of the equilibrium spring (lower spring) and the spring in the fractional Maxwell arm (upper spring). Giraldo-Londoño et al. [53] used a fractional viscoelastic model such as that in Fig. 3, together with a damage element, to model rate-dependent fracture behavior of polymers with a high level of accuracy across a wide range of loading rates.

The equation that determines the mechanical behavior of a fractional SLS is:

$$ \sigma(t) + \hat{\lambda}\ {}_0D_t^{\hat{v}}\sigma(t) = E\varepsilon(t) + \hat{\gamma}\ {}_0D_t^{\hat{v}}\varepsilon(t), \tag{22} $$

where

$$ \hat{\lambda} = \hat{\eta}/cE, \quad \text{and} \quad \hat{\gamma} = \hat{\lambda}(1+c)E. \tag{23} $$

Eq. (22) is referred to as a fractional differential equation because it is defined in terms of fractional differential operators. In order to obtain the complex modulus of the fractional SLS model, we apply the Fourier transform to

[2] Fractional calculus is a branch of calculus that studies the meaning and implications of differential operators of non-integer order [48–50].

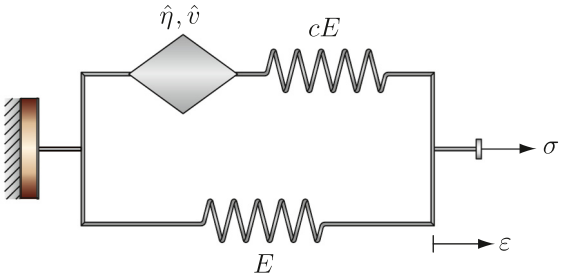

Fig. 3. Fractional standard linear solid model.

the fractional differential equation (22), yielding:[3]

$$E^*(\omega) = \frac{E + \hat{\gamma}\,(i\omega)^{\hat{v}}}{1 + \hat{\lambda}\,(i\omega)^{\hat{v}}}. \tag{24}$$

We use de Moivre's theorem to rewrite Eq. (24) in the form

$$E^*(\omega) = E'(\omega) + i\,E''(\omega), \tag{25}$$

where

$$\begin{aligned} E'(\omega) &= \frac{E + \hat{\gamma}\hat{\lambda}\omega^{2\hat{v}} + (E\hat{\lambda} + \hat{\gamma})\omega^{\hat{v}} \cos \hat{v}\pi/2}{1 + \hat{\lambda}^2\,\omega^{2\hat{v}} + 2\hat{\lambda}\omega^{\hat{v}} \cos \hat{v}\pi/2} \quad \text{and} \\ E''(\omega) &= \frac{(\hat{\gamma} - E\hat{\lambda})\omega^{\hat{v}} \sin \hat{v}\pi/2}{1 + \hat{\lambda}^2\,\omega^{2\hat{v}} + 2\hat{\lambda}\omega^{\hat{v}} \cos \hat{v}\pi/2} \end{aligned} \tag{26}$$

are the storage and loss moduli of the material, respectively. Assuming a frequency-independent Poisson's ratio,[4] we use the storage and loss moduli given in Eq. (26) to obtain the complex modulus tensor for each candidate material, which we then use to obtain the homogenized complex modulus tensor through Eqs. (4)–(5).

4. Modified ZPR design variable update scheme

Zhang et al. [29] introduced an efficient design variable update scheme, called ZPR (named after initials of the authors' last names: Zhang–Paulino–Ramos Jr.), and applied it to the design of nonlinear multi-material truss structures. The ZPR (phonetically, *zipper*) design variable scheme by Zhang et al. [29] exploits the fact that, if each design variable is associated with a single constraint, then all design variables associated with a constraint can be updated independently of the other constraints, and the update rule can be found in a similar way as in the optimality criteria (OC) method [56,57]. The ZPR scheme is an efficient design variable update scheme, but it is limited to the solution of self-adjoint problems.

To solve non-self-adjoint problems, Giraldo-Londoño et al. [58] adopted the approach by Zhang et al. [29] and used the sensitivity separation concept by Jiang et al. [59] to develop an efficient design variable update scheme tailored to solve topology optimization problems with a general setting of constraints and for an objective function with sensitivities of unrestricted sign. Similarly to the Convex Linearization method (CONLIN) [60,61] and the MMA family [62,63], our method treats the positive and negative components of the sensitivity of the objective in a separate way. To update the design variables at optimization iteration k, we first introduce the non-monotonous convex approximation of the objective function:

$$\tilde{J}(\mathbf{z}_1, \ldots, \mathbf{z}_m) = J(\mathbf{z}_1^k, \ldots, \mathbf{z}_m^k) + \sum_{i=1}^{m} \{\mathbf{a}_i^T [\mathbf{y}_i(\mathbf{z}_i) - \mathbf{y}_i(\mathbf{z}_i^k)] + \mathbf{b}_i^T (\mathbf{z}_i - \mathbf{z}_i^k)\}, \tag{27}$$

[3] Noticing from Eq. (20) that ${}_0D_t^{\hat{v}} f(t) = \frac{t^{-\hat{v}}}{\Gamma(1-\hat{v})} * \frac{\mathrm{d}f(t)}{\mathrm{d}t}$, it follows that the Fourier transform of the fractional derivative of a function $f(t)$ is $\mathcal{F}\{{}_0D_t^{\hat{v}} f(t)\}(\omega) = (i\omega)^{\hat{v}}\mathcal{F}\{f(t)\}(\omega)$ [54].

[4] Poisson's ratio is, in general, time (or frequency) dependent. However, we neglect its effect because, for most materials, the relaxation of Poisson's ratio is negligible when compared to the relaxation of stiffness [55].

where

$$\begin{aligned}
&\mathbf{y}_i(\mathbf{z}_i) = \mathbf{z}_i^{-\alpha}, \quad i = 1 \dots m, \quad \alpha > 0, \\
&a_i^e = \frac{\partial J^-}{\partial y_i^e}(\mathbf{z}_1^k, \dots, \mathbf{z}_m^k) = -\frac{1}{\alpha}\left(z_i^{e,k}\right)^{1+\alpha} \frac{\partial J^-}{\partial z_i^e}(\mathbf{z}_1^k, \dots, \mathbf{z}_m^k) \geq 0, \quad e = 1, \dots, N_e, \\
&b_i^e = \frac{\partial J^+}{\partial z_i^e}(\mathbf{z}_1^k, \dots, \mathbf{z}_m^k) \geq 0, \quad e = 1, \dots, N_e, \quad \text{and} \\
&\frac{\partial J}{\partial z_i^e} = \frac{\partial J^+}{\partial z_i^e} + \frac{\partial J^-}{\partial z_i^e}.
\end{aligned} \tag{28}$$

The form of the convex approximation (27) was first used for single-material topology optimization in a study by Jiang et al. [59], who called it *sensitivity separation* because the sensitivity of the objective with respect to a design variable is separated into a positive and a negative term (i.e., $\partial J/\partial z_i^e = \partial J^+/\partial z_i^e + \partial J^-/\partial z_i^e$, with $\partial J^+/\partial z_i^e \geq 0$ and $\partial J^-/\partial z_i^e \leq 0$). The non-monotonous convex function (27) is well-defined only if $\partial J^+/\partial z_i^e \geq 0$ and $\partial J^-/\partial z_i^e \leq 0$. Giraldo-Londoño et al. [58] defined the positive and negative components of the sensitivity such that the second order derivatives of the convex approximation (27) approximate those of the original objective function, $J(\mathbf{z}_1, \dots, \mathbf{z}_m)$. The expressions for $\partial J^+/\partial z_i^e \geq 0$ and that $\partial J^-/\partial z_i^e \leq 0$ derived in their study are as follows:

$$\frac{\partial J^-}{\partial z_i^e} = \min\left\{-\frac{|h_i^{e,k}| z_i^{e,k}}{\alpha + 1}, \frac{\partial J}{\partial z_i^e}\right\}, \qquad \frac{\partial J^+}{\partial z_i^e} = \frac{\partial J}{\partial z_i^e} - \frac{\partial J^-}{\partial z_i^e}, \tag{29}$$

where $h_i^{e,k}$ are estimates of the second-order derivatives of the objective function at iteration k. To obtain these estimates, Giraldo-Londoño et al. [58] used a diagonal approximation of the Hessian matrix inspired by the BFGS method [64–67]. However, in the current study we found that a diagonal approximation of the Hessian matrix based on the Powell Symmetric Broyden (PSB) quasi-Newton update [68,69] is more suitable than the diagonal approximation based on the BFGS method. The approximation used in this study is given by

$$\mathbf{h}_k = \mathbf{h}_{k-1} + \frac{\mathbf{c}_k^T \mathbf{s}_k - \mathbf{h}_{k-1}^T \mathbf{s}_k^2}{(\mathbf{s}_k^2)^T \mathbf{s}_k^2} \mathbf{s}_k^2, \tag{30}$$

where:

$$\begin{aligned}
&\mathbf{h}_k = [h_1^{1,k}, \dots, h_1^{N_e,k}, \dots, h_m^{1,k}, \dots, h_m^{N_e,k}]^T, \\
&\mathbf{c}_k = \left.\frac{\partial J}{\partial \mathbf{z}}\right|_{\mathbf{z}=\mathbf{z}^k} - \left.\frac{\partial J}{\partial \mathbf{z}}\right|_{\mathbf{z}=\mathbf{z}^{k-1}}, \\
&\mathbf{s}_k = \mathbf{z}^k - \mathbf{z}^{k-1}, \quad \text{and} \\
&\mathbf{z} = [z_1^1, \dots, z_1^{N_e}, \dots, z_m^1, \dots, z_m^{N_e}]^T.
\end{aligned} \tag{31}$$

To obtain the ZPR-based design variable update scheme based on the sensitivity separation, we solve the following approximate sub-problem at each optimization iteration, k:

$$\begin{aligned}
\min_{\mathbf{z}_1, \dots, \mathbf{z}_m} \quad & \tilde{J}(\mathbf{z}_1, \dots, \mathbf{z}_m) = \sum_{i=1}^{m} [\mathbf{a}_i^T \mathbf{y}_i(\mathbf{z}_i) + \mathbf{b}_i^T \mathbf{z}_i] \\
\text{s.t.} \quad & g_j(\mathbf{z}_1, \dots, \mathbf{z}_m) = g_j(\mathbf{z}_1^k, \dots, \mathbf{z}_m^k) + \sum_{i \in \mathcal{M}_j} \sum_{e \in \mathcal{E}_j} \frac{\partial g_j}{\partial z_i^e}(z_i^e - z_i^{e,k}) \leq 0, \quad j = 1, \dots, N_c \\
& z_{i,L}^{e,k} \leq z_i^e \leq z_{i,U}^{e,k}, \quad e = 1, \dots, N_e, \quad i = 1, \dots, m,
\end{aligned} \tag{32}$$

where

$$z_{i,L}^{e,k} = \max(z_{\min}, z_i^{e,k} - \text{move}) \quad \text{and} \quad z_{i,U}^{e,k} = \min(1, z_i^{e,k} + \text{move}), \tag{33}$$

and "move" refers to the move limit.

The solution of the approximate sub-problem yields the following design variable update rule:

$$z_i^e(\lambda_j) = \begin{cases} z_{i,L}^e, & \text{if } B_i^e(\lambda_j) \leq z_{i,L}^{e,k}, \\ B_i^e(\lambda_j), & \text{if } z_{i,L}^{e,k} < B_i^e(\lambda_j) < z_{i,U}^{e,k} \\ z_{i,U}^e, & \text{if } B_i^e(\lambda_j) \geq z_{i,U}^{e,k}, \end{cases} \tag{34}$$

where

$$B_i^e(\lambda_j) = z_i^{e,k} \left[\frac{-\frac{\partial J^-}{\partial z_i^e}(\mathbf{z}_1^k, \ldots, \mathbf{z}_m^k)}{\frac{\partial J^+}{\partial z_i^e}(\mathbf{z}_1^k, \ldots, \mathbf{z}_m^k) + \lambda_j \frac{\partial g_j}{\partial z_i^e}(\mathbf{z}_1^k, \ldots, \mathbf{z}_m^k)} \right]^{\frac{1}{1+\alpha}} \tag{35}$$

and λ_j is the Lagrange multiplier associated with constraint g_j. As shown by Eqs. (34)–(35), the update of a design variable only depends on the Lagrange multiplier of the constraint to which it is associated. As a result, all design variables that belong to a constraint can be updated at once and independent of the design variables associated with a different constraint. The final part of the update scheme consists of obtaining the Lagrange multipliers from Eq. (35), which we find from the solution of the dual problem associated with the approximate sub-problem (32). That is, to obtain the Lagrange multipliers, λ_j, we solve

$$g_j(\mathbf{z}_1^k, \ldots, \mathbf{z}_m^k) + \sum_{i \in \mathcal{M}_j} \sum_{e \in \mathcal{E}_j} \frac{\partial g_j}{\partial z_i^e} (z_i^e(\lambda_j) - z_i^{e,k}) = 0, \tag{36}$$

which we do using the bisection method. Given that (34)–(36) share similarities with the OC method, the update of the design variables using the present approach becomes relatively inexpensive.

In our implementation, we compute the updated design variables using a damping scheme, as

$$\mathbf{z}_i^k = \zeta \mathbf{z}_i^k + (1 - \zeta)\mathbf{z}_i^{k-1}, \quad i = 1, \ldots, m, \tag{37}$$

where $0 < \zeta < 1$ is a damping parameter and $\mathbf{z}_i^k$ and $\mathbf{z}_i^{k-1}$ are the vectors of design variables at iterations k and $k-1$, respectively. The damping scheme reduces fluctuations of the objective function during consecutive optimization iterations, which tend to happen in the initial steps, when the diagonal approximation of the Hessian is not accurate.

5. Implementation

This section describes some of the implementation details related to the solution of the optimization problem discussed previously. First, we provide details of the computation of the complex stiffness matrices necessary to obtain the homogenized complex modulus tensor and finalize with a description of the topology optimization flowchart for the design of multi-phase viscoelastic materials.

5.1. Computational homogenization of the complex modulus tensor

As discussed in Section 2, the homogenized complex modulus tensor is obtained by solving the periodic boundary problem (5) and then using Eq. (4). In this study, we solve the periodic boundary value problem (5) using the finite element method and obtain the homogenized complex modulus tensor using its representation in terms of mutual energies shown in Eq. (15). The homogenized complex modulus is approximated in terms of the element displacement vectors, $\mathbf{u}_e^{A(ij)}$, associated with the strain fields, $(\bar{\varepsilon}_{pq}^{(ij)} - \tilde{\varepsilon}_{pq}^{(ij)})$, and the element stiffness matrices, $\mathbf{k}_e^*$, similar to what Xia and Breitkopf [70] used for the homogenization of linear elastic materials. That is, we obtain the homogenized complex modulus tensor numerically as follows:

$$E_{ijkl}^{*H} = \frac{1}{|Y|} \sum_{e=1}^{N_e} (\mathbf{u}_e^{A(ij)})^T \mathbf{k}_e^* \mathbf{u}_e^{A(ij)}. \tag{38}$$

Note that, unlike the element stiffness matrices for elastic materials, the element stiffness matrices, $\mathbf{k}_e^*$, in (38) are complex. Therefore, they are divided into a real part, $\mathbf{k}_e^R$, associated with the storage modulus, and an imaginary part, $\mathbf{k}_e^I$, associated with the loss modulus, as follows:

$$\mathbf{k}_e^* = \mathbf{k}_e^R + i\mathbf{k}_e^I, \tag{39}$$

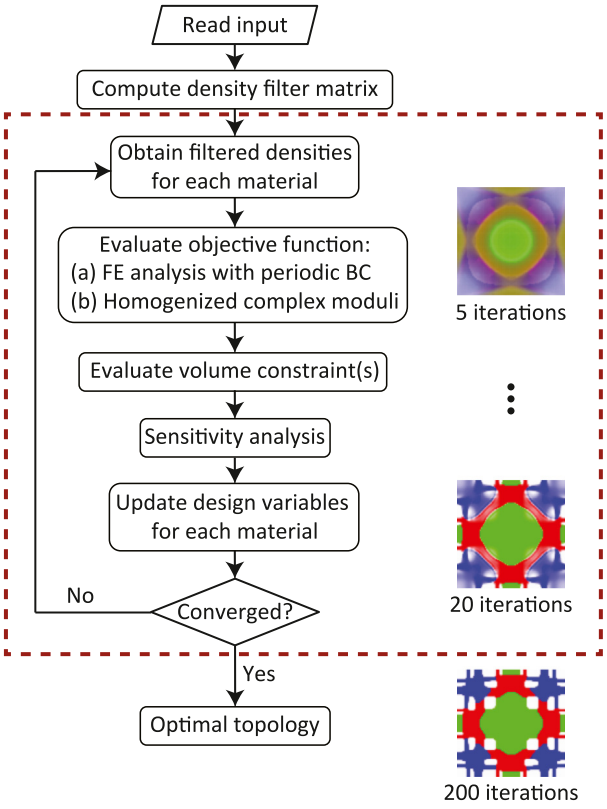

Fig. 4. Flowchart showing the topology optimization steps for the design of multi-material viscoelastic microstructures.

where $\mathbf{k}_e^R$ and $\mathbf{k}_e^I$ are obtained as

$$\mathbf{k}_e^R = \int_{\Omega_e} \mathbf{B}^T \mathbf{D}^R \mathbf{B} \mathrm{d}V \quad \text{and} \quad \mathbf{k}_e^I = \int_{\Omega_e} \mathbf{B}^T \mathbf{D}^I \mathbf{B} \mathrm{d}V. \tag{40}$$

$\mathbf{D}^R$ and $\mathbf{D}^I$ are the constitutive matrices for an isotropic material, which we obtain using the effective storage and loss modulus of element e, respectively (see Eq. (13)), $\mathbf{B}$ is the classical strain/displacement matrix, and Ω_e is the domain defining element e.

5.2. Topology optimization steps for the design of multi-material viscoelastic microstructures

This section shows the basic steps used in the design of multi-material viscoelastic microstructures. The flowchart shown in Fig. 4 describes the main steps used in this study to solve the topology optimization statement (6). As seen in the flowchart, the density filter matrix is computed after reading the input data (e.g., FE mesh, material properties, design frequency, stopping criteria, and filter radius). The computation of the filter matrix is followed by the main optimization iterations (see dashed box). Inside the main loop, the homogenized complex modulus tensor is obtained and used to compute the objective function. After this computation, the volume constraints are obtained. Because we use a gradient-based optimization approach, sensitivity information of both the objective function and the volume constraints, is needed. These are used to update the design variables via the modified ZPR design variable update scheme discussed in Section Section 4. The loop continues until convergence is achieved. A more detailed description of the optimization steps is shown in Algorithm 1.

6. Numerical results

We use the topology optimization formulation introduced previously to solve two problems of interest. The first problem aims to maximize the homogenized loss modulus of the material for a given target frequency and the

Algorithm 1 Topology optimization of multi-material viscoelastic microstructures

Initialize: $\texttt{Change} = 1,\ k = 0,\ \mathbf{z}_1^k, \ldots, \mathbf{z}_m^k$
while ($k \leq \texttt{MaxIter}$ and $\texttt{Change} > \texttt{Tol}$) **do**
  Solve periodic BVP (5) using FEM and evaluate E_{ijkl}^{*H} using Eq. (38)
  Compute $J(\mathbf{z}_1^k, \ldots, \mathbf{z}_m^k)$, and $g_j \quad (j = 1, \ldots, N_c)$ as shown in (6)
  Evaluate sensitivity of the objective function using Eqs. (18)–(19)
  Evaluate sensitivity of the constraints
  Update design variables $(\mathbf{z}_1^{k+1}, \ldots, \mathbf{z}_m^{k+1})$ using Eqs. (34)–(37)
  Compute $\texttt{Change} = \max\left(\|\mathbf{z}_1^{k+1} - \mathbf{z}_1^k\|_\infty, \ldots, \|\mathbf{z}_m^{k+1} - \mathbf{z}_m^k\|_\infty\right)$
  Set $k \leftarrow k + 1$
end while
Plot final topology

Table 1
Material properties for the three candidate viscoelastic materials.

Material	E (MPa)	c	$\hat{v}$	$\hat{\eta}$ (MPa $s^{\hat{v}}$)
1	1	5	0.9	20
2	1	5	0.9	3
3	1	5	0.9	0.5

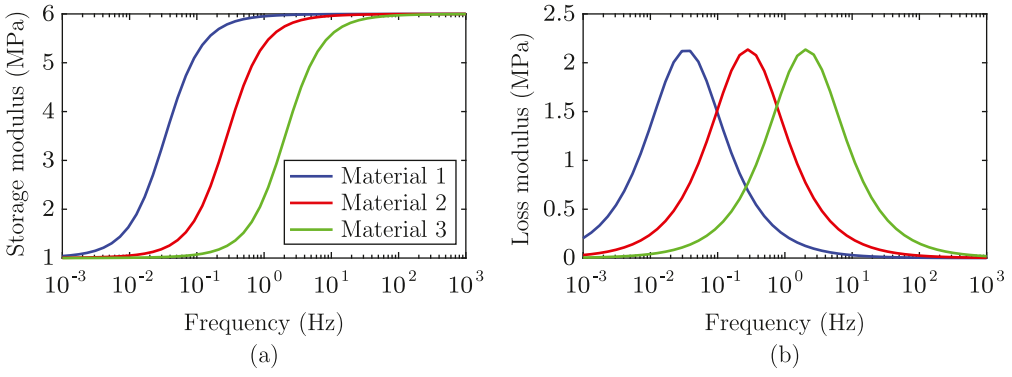

Fig. 5. Viscoelastic behavior of the materials in Table 1 as a function of frequency: (a) storage modulus and (b) loss modulus.

second problem aims to obtain microstructures with tailored loss modulus for a set of target frequencies. For the sake of illustration, all designs shown in this section consider three candidate materials, whose viscoelastic properties are shown in Table 1. The storage and loss modulus for each material phase are obtained from Eqs. (26) and are depicted in Fig. 5.

Unless otherwise specified, we use the parameters from Table 2 to solve all problems in the present study. Moreover, for all examples presented in this section, we discretize the unit cell using 100×100 regular quadrilateral finite elements for 2D microstructures and $70 \times 70 \times 70$ regular hexahedral elements for 3D microstructures. The initial density distribution for each material phase is chosen as $z_i^e = c \times 1/2(\sin(\pi x_e/L) + \sin(\pi y_e/L))$ for 2D microstructures and $z_i^e = c \times 1/3(\sin(\pi x_e/L) + \sin(\pi y_e/L) + \sin(\pi z_e/L))$ for 3D microstructures, where $i = 1, \ldots, m$, $e = 1, \ldots, N_e$, $(x_e,\ y_e,\ z_e)$ are the coordinates of the centroid of element e, L is the size of the unit cell, and c is a constant chosen to satisfy the volume constraints at the beginning of the optimization iterations. A non-uniform density distribution is necessary to design material microstructures in order to prevent all sensitivities from being identical, which leads to designs with zero densities in all elements.

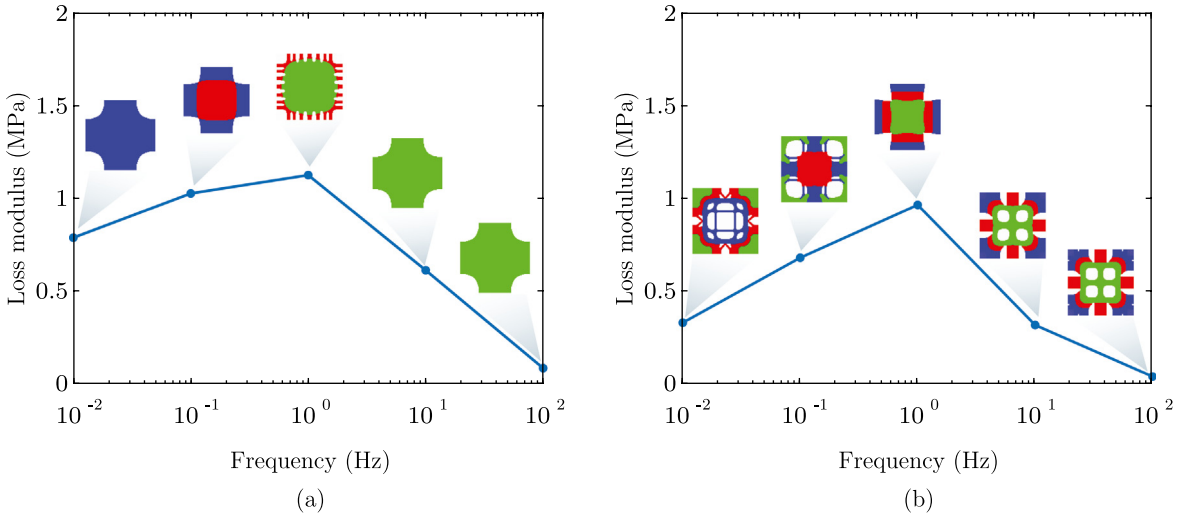

Fig. 6. Effect of the design frequency on the optimized 2D microstructures: The results in (a) use volume constraint (41) with $\bar{v}_1 = 0.75$ and those in (b) use volume constraints (42) with $\bar{v}_j = 0.25, \quad j = 1, \ 2, \ 3$.

6.1. Maximization of loss modulus for a single target frequency

6.1.1. Effect of design frequency

First, we study the effect of the design frequency in the optimized topology of the unit cell. In addition to varying the design frequency, we consider two types of volume constraints. The first type of volume constraint specifies a single volume fraction limit, $\bar{v}_1 = 0.75$, such that the volume occupied by all three candidate materials does not exceed 75% of the design domain volume. Mathematically, this volume constraint is expressed as

$$g_1 = \frac{\sum_{i=1}^{m} \sum_{e=1}^{N_e} v_e \rho_i^e}{|Y|} - \bar{v}_1 \leq 0, \tag{41}$$

where $|Y| = L^2$ for 2D microstructures and $|Y| = L^3$ for 3D microstructures, in which L is the size of the unit cell. To recast volume constraint (41) in the format shown in (6), we use $\mathcal{M}_1 = \{1, \ldots, m\}$ and $\mathcal{E}_1 = \{1, \ldots, N_e\}$.

The second type of volume constraint specifies a maximum volume of 25% to each of the three candidate materials, such that the three materials can fill up to 75% of the design domain volume. This type of volume constraint is mathematically expressed as

$$g_j = \frac{\sum_{e=1}^{N_e} v_e \rho_j^e}{|Y|} - \bar{v}_j \leq 0, \quad j = 1, \ldots, 3. \tag{42}$$

That is, the set of candidate materials associated with volume constraint j is $\mathcal{M}_j = j$, and the set of elements associated with constraint j is $\mathcal{E}_j = \{1, \ldots, N_e\}$. For this case, we specify volume fraction limits, $\bar{v}_j = 0.25, \quad j = 1, \ldots, 3$.

We obtain optimized microstructural topologies for design frequencies ranging from 10^{-2} Hz to 10^2 Hz and display the results in Fig. 6a for volume constraint (41) and in Fig. 6b for volume constraint (42). From the results, we observe that for both volume constraint settings, materials with larger loss modulus (i.e., those with more energy dissipation capabilities) are placed closer to the core of the unit cell than those with smaller loss modulus (i.e., those with less energy dissipation capabilities). In contrast to the results obtained with volume constraint (42), not all materials appear in the results obtained with volume constraint (41). For instance, for the designs obtained with volume constraint (42), a design frequency of 10^{-2} Hz yields only material 1 (the most dissipative for that frequency) and a design frequency of 10^{-1} Hz yields only materials 1 and 2 (the two most dissipative materials for that frequency).

When comparing the results from Fig. 6a and b, we also observe that the optimized loss modulus for volume constraint (41) is always larger than that for volume constraint (42). That is because, in contrast to the second

Table 2
Numerical parameters used to solve all problems in the present study.

Parameter	Description	Value
ξ	Weight factor	1
δ	Mass penalization factor	1
h_e	Element size	1
R	Filter radius	2
q	Filter exponent	1 (2D), 2 (3D)
`MaxIter`	Maximum number of iterations[a]	{25,25,500}
p_R	DMO penalization parameter for storage modulus[a]	{1,1,3}
p_I	DMO penalization parameter for loss modulus[a]	{2,2,4}
γ	Mixing penalty parameter[a]	{0,0.5,1}
η	Threshold projection density	0.5
β	Penalization of threshold projection function[b]	{1,2,3,4,5}
`Tol`	Tolerance	0.0005 (2D), 0.001 (3D)
α	Design variable update scheme parameter	1
ζ	Damping parameter	0.5
$\mathbf{h}_0$	Initial diagonal Hessian estimation	$\mathbf{0}$
`move`	Move limit	0.3
$z_{\min}$	Design variable lower bound	0
ϵ	Ersatz stiffness	10^{-4}

[a]We consider three continuation steps, such that `MaxIter` = 25 for the first two continuation steps and `MaxIter` = 500 for the third. The DMO penalization parameters, p_R and p_I, and the mixing penalty parameter, γ, are updated at each continuation step.
[b]Parameter β starts at 1 and, during the last continuation step, is increased by one every 30 iterations until reaching a maximum value, $\beta_{\max} = 5$.

volume constraint setting, the first only imposes one global constraint to the entire design domain. In other words, the solution space for the first constraint setting is larger than that for the second constraint setting, and thus, the optimizer can find a better local optima for the first.

Fig. 7 shows the optimization results for design frequencies of 0.1 Hz and 1 Hz and for volume constraint (41). The first column of Fig. 7 shows the design frequencies, the second and third columns show the unit cell and a 3 × 3 array of the unit cell, respectively, and the last column shows the homogenized loss modulus of the optimized microstructures as a function of frequency. For each design frequency, volume constraint (41) is active, but the optimized topologies are significantly different. That is, each design uses the same amount of material, but its distribution is such that it maximizes the material loss modulus for the given design frequency. The effect of this material distribution on the homogenized behavior of the viscoelastic composite is observed in the homogenized loss modulus plots shown in the last column of Fig. 7. From these plots, we observe that the loss modulus of the optimized materials increases in the vicinity of the design frequency.

For volume constraint (41), one would expect that the optimizer will choose the material with largest loss modulus for a given design frequency. However, as illustrated in Figs. 6a and 7, that is not always the case. The results show that, depending on the design frequency, a design may contain more than one material. For instance, although the results in Fig. 7 are obtained for a single frequency, the optimized topologies contain two materials. When the design frequency is 0.1 Hz, the optimizer chooses materials 1 and 2, which are those with largest lost modulus for that design frequency. Likewise, when the design frequency is 1 Hz, the optimizer chooses materials 2 and 3 because those are the materials with largest loss modulus for that frequency.

Fig. 8 shows the optimization results for design frequencies of 0.1 Hz and 1 Hz and for volume constraint (42). Unlike the results shown in Fig. 7, those in Fig. 8 contain all three candidate materials, which happens because each of the constraints in (42) is applied to one of the candidate materials. Although constraint (42) is more restrictive than constraint (41), the optimizer is still able to find an optimized topology for each of the candidate materials to maximize the loss modulus at each of the target frequencies.

Besides the 2D results discussed above, we also obtain optimized topologies for 3D microstructures. Fig. 9 shows the optimization results obtained for two design frequencies (0.1 Hz and 1 Hz) and for the two volume constraint settings considered previously. The 3D results also show that a single volume constraint may lead to more than one

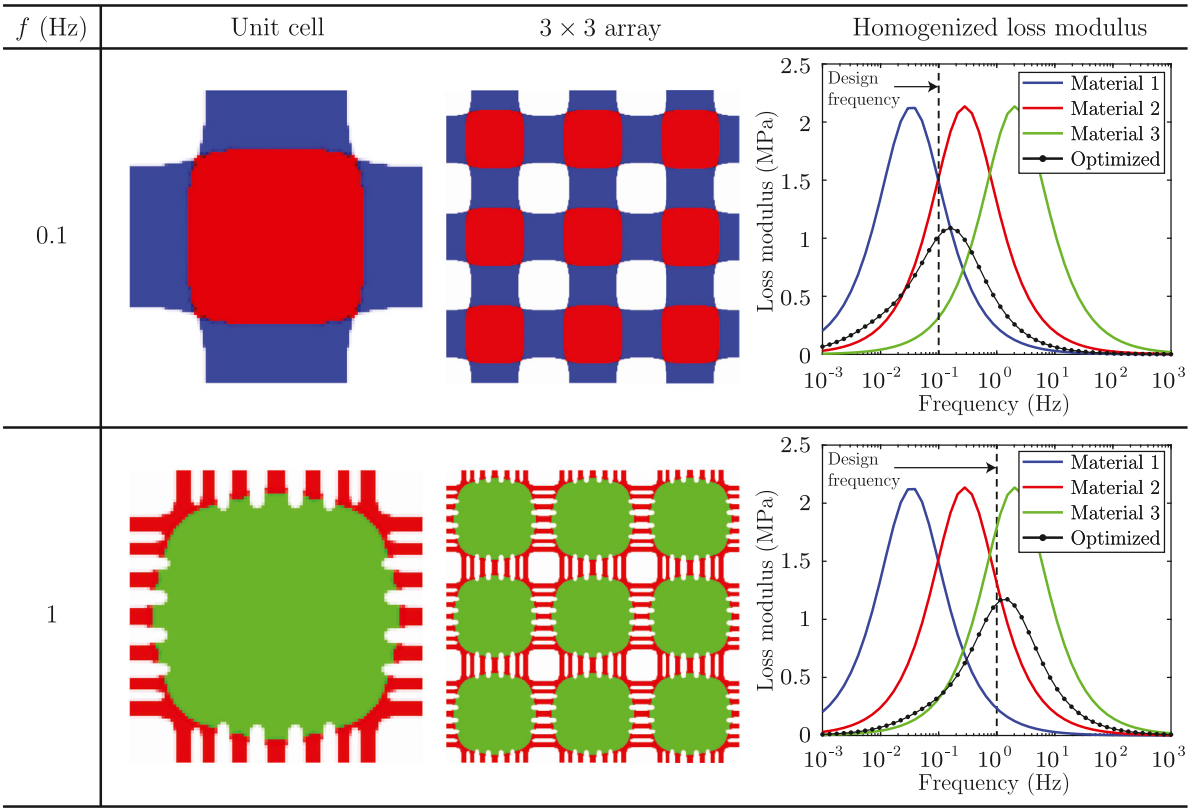

Fig. 7. Effect of the design frequency in the optimized topology of the unit cell considering volume constraint (41) with $\bar{v}_1 = 0.75$.

material appearing in the optimized topology of the unit cell. As expected, the optimized loss modulus obtained with one global volume constraint (Figs. 9a-b) is larger than that obtained with three volume constraints (Figs. 9c-d). To visualize the interior of each unit cell in detail, we removed an octant from their geometry, as depicted in Fig. 10. Similarly to the 2D results, here we also observe that the optimizer places the most dissipative material for a given target frequency toward the center of the unit cell.

6.1.2. Effect of volume fraction limit

Now, we study the effect of increasing the volume fraction limit on the optimized topology of the unit cell. To this end, we fix the design frequency and vary the volume fraction limit, using the volume constraint settings in (41) and (42). For volume constraint (41) we choose $\bar{v}_1 = \bar{v}$, and for volume constraint (42) we choose $\bar{v}_j = \bar{v}/3,\ j = 1, \ldots, 3$, where $\bar{v}$ is the prescribed total volume fraction limit. The results are shown in Fig. 11, in which those corresponding to volume constraint (41) are given in Figs. 11a-b and those corresponding to volume constraint (42) are given in Figs. 11c-d.

First, we note that the material distribution depicted in Fig. 11 closely follows that observed in Figs. 7 and 8. That is, the material with largest loss modulus is concentrated toward the core of the unit cell and those with smaller loss modulus are placed away from it. Additionally, we observe that the loss modulus of the optimized microstructure increases nonlinearly as the material volume fraction increases. Finally, Fig. 11 shows that the optimized loss modulus considering volume fraction (41) is larger than the optimized loss modulus considering volume fraction (42), as expected.

6.2. Tailoring of energy dissipation for a set of target frequencies

Here, we design microstructures with a tailored loss modulus for a given set of design frequencies. For the designs shown here, we consider volume constraint (41) with a volume fraction limit $\bar{v}_1 = 1$ and let the optimizer choose

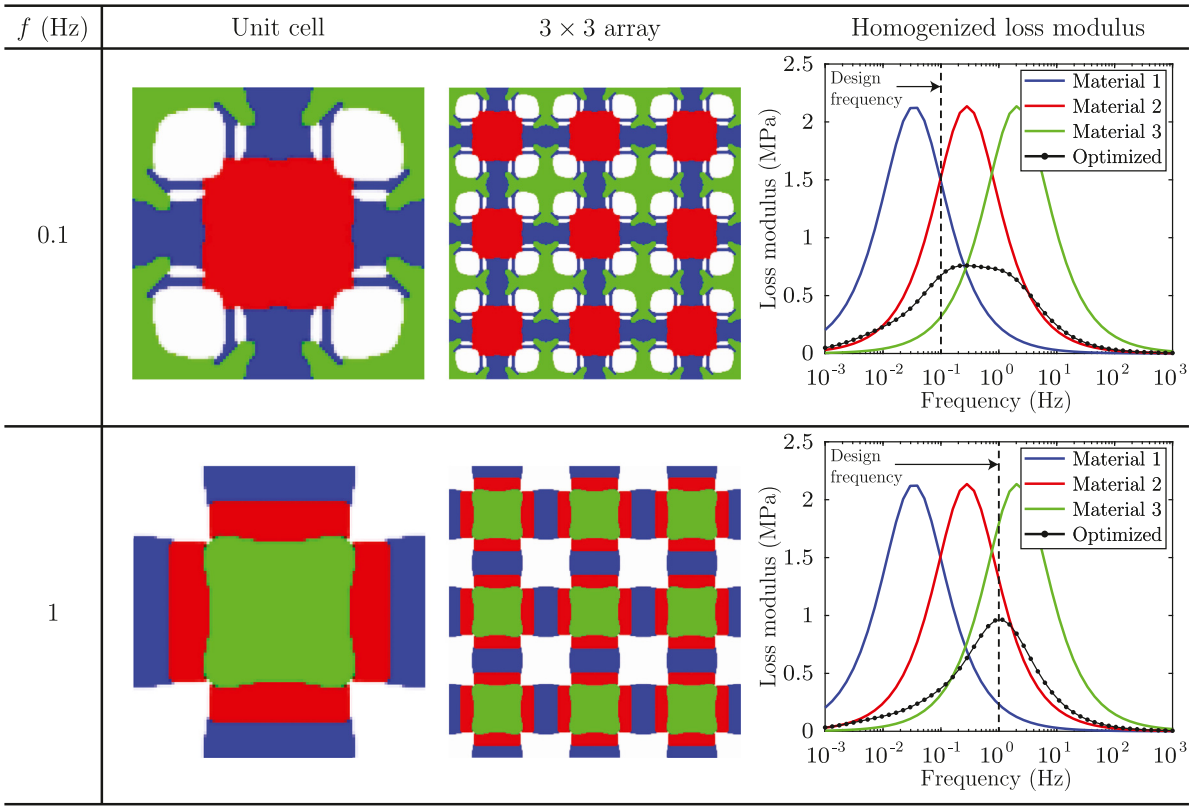

Fig. 8. Effect of the design frequency in the optimized topology of the unit cell considering volume constraints (42) with $\bar{v}_j = 0.25, \quad j = 1, \ldots, 3$.

Table 3
Target loss moduli used for the design of microstructures with tailored energy dissipation behavior.

Target frequency, ω_i (Hz)	Target loss modulus, $E''(\omega_i)$ (MPa)			
	Case 1	Case 2	Case 3	Case 4
0.03	0.5	0.75	0.25	0.75
0.3	0.5	0.5	0.5	0.5
3	0.5	0.25	0.75	0.75

the right amount of each material to achieve the desired viscoelastic behavior. We present four different designs, each corresponding to a different set of target loss moduli for the same set of target frequencies, as presented in Table 3. The goal of this example is to illustrate how the same number of fixed candidate materials can be arranged in different topological configurations to achieve a desired energy dissipation behavior.

Fig. 12 shows the 2D designs obtained for each of the cases shown in Table 3. Depending on the design case, the optimizer selects an appropriate subset of materials, so that the homogenized loss modulus of the optimized microstructure approximates the target loss modulus at each of the target frequencies. For instance, in case 1, the optimizer selects materials 1 and 2, leading to a microstructure whose loss modulus has a plateau-like behavior for the range of design frequencies. In case 2, the optimizer selects all three materials, but it contains a larger amount of material 1, such that the microstructure has a larger loss modulus for lower frequencies (e.g., for frequencies

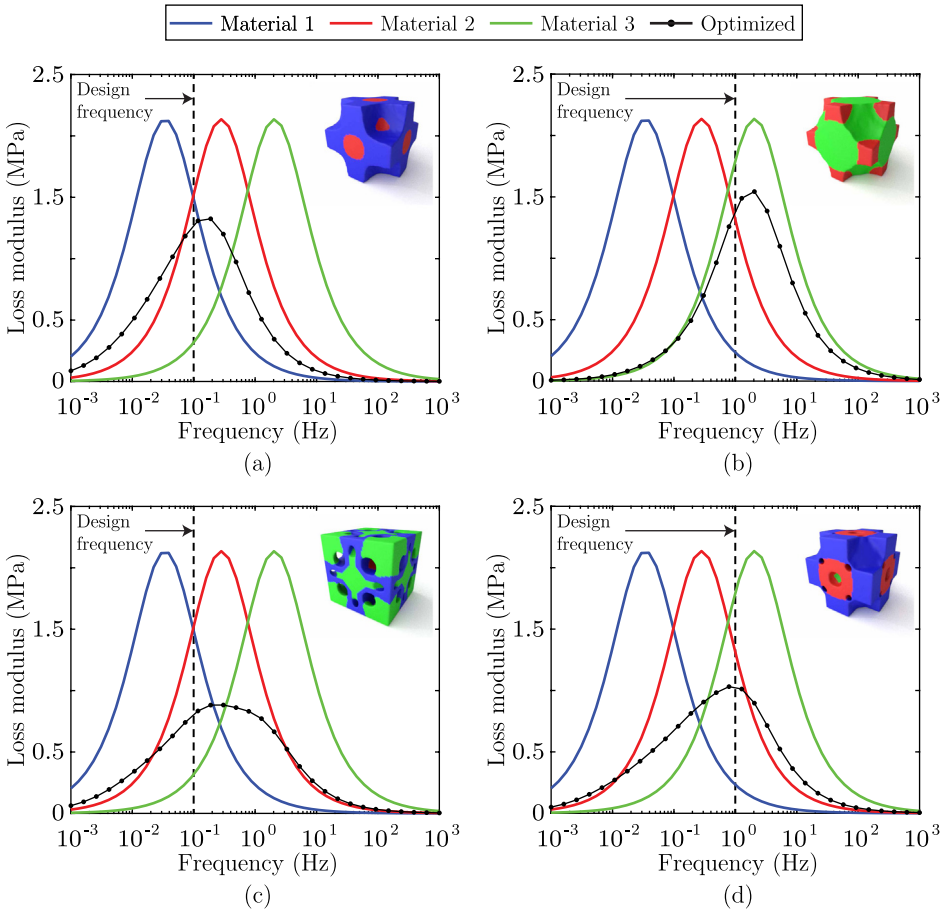

Fig. 9. Effect of the design frequency and volume constraint setting in the optimized topology of 3D unit cells: (a) and (b) are obtained using volume constraint (41) with $\bar{v}_1 = 0.75$ and design frequencies of 0.1 Hz and 1 Hz, respectively, and (c) and (d) are obtained using volume constraint (42) with $\bar{v}_j = 0.25$ and design frequencies of 0.1 Hz and 1 Hz, respectively.

close to 0.03 Hz) than that for higher frequencies. Conversely, in case 3, the optimizer selects a larger amount of material 3 to yield a loss modulus that increases when the frequencies approach 3 Hz. Finally, in case 4, the optimizer selects once more materials 1 and 2, but this time the topology is such that it leads to a microstructure with a loss modulus that becomes smaller when the frequency approaches 0.3 Hz.

In addition to the 2D designs, we obtain optimized 3D microstructures, as depicted in Fig. 13. As shown by the results, the optimizer is able to select the right amount of each of the three candidate materials in order to achieve the desired target loss moduli for the given set of design frequencies. We present a more detailed view of the interior of each unit cell by removing an octant from their geometry, which we show in Fig. 14.

7. Computational efficiency

We study the efficiency of the formulation via a computational cost analysis of some of the results from the previous section.[5] To assess the efficiency of the design variable update scheme, we also compare the computational cost obtained using the modified ZPR scheme with that obtained using MMA.

[5] The computational costs displayed in this section were obtained using Matlab R2017b on a desktop computer with an Intel(R) Xenon(R) CPU E5-1660 v3 at 3.00 GHz and 256 GB of RAM running on a 64-bit operating system.

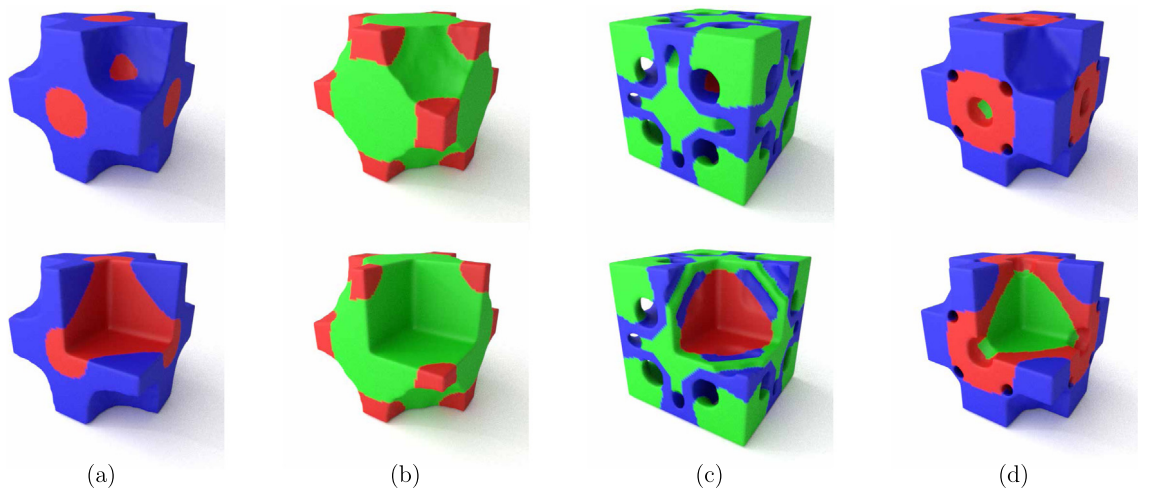

Fig. 10. Optimized topologies of 3D unit cells shown in Fig. 9. Figures (a) and (b) correspond to designs obtained with volume constraint (41) and design frequencies of 0.1 Hz and 1 Hz, respectively, and figures (c) and (d) to those obtained with volume constraint (42) and design frequencies of 0.1 Hz and 1 Hz, respectively. As shown in the bottom row figures, we have removed an octant from the geometry of each cell to display their interior in detail.

Fig. 15 displays the percentual breakdown of computational cost for a subset of the results from Figs. 7, 8, and 12. The results on the left hand side correspond to the design on the first row of Fig. 7, those on the center to the design on the first row of Fig. 8, and those on the right hand side to the design on the first row of Fig. 12. In all cases, the percent of total time required to update the design variables using MMA is considerably larger than that required using our design variable update scheme. The percent of total time to update the design variables obtained using our approach falls below 1%, while that obtained using MMA ranges between 4% and 18%. The smallest percent time required by MMA (4%) corresponds to the case in which we design for a tailored loss modulus behavior, which is expected because for that case we need to solve a large amount of periodic boundary value problems in order to homogenize the complex modulus tensor for the three target frequencies. Regardless, the absolute time required by MMA to update the design variables for that case ($\sim$1 min) is much larger than that required by our update scheme ($\sim$4 s).

8. Concluding remarks

We have introduced a framework for the design of periodic multi-material viscoelastic composites with maximized loss modulus for a single target frequency or with tailored energy dissipation for a range of frequencies. The viscoelastic behavior of each candidate material is represented by a fractional standard linear solid model, a type of rheological model based on fractional differential operators, which is capable of simulating the behavior of viscoelastic materials accurately with a few amount of input parameters. To tailor the viscoelastic response of the composite, we use a set of control points, each corresponding to the desired loss modulus of the material for a given target frequency. The optimization statement is setup to find the lightest microstructure that minimizes the sum of squared loss modulus residuals, in which the residual at a given frequency is defined as the difference between the homogenized loss modulus and the target loss modulus evaluated at that frequency. To obtain lightweight microstructures, we write the objective function as a weighted sum between the sum of squared residuals and the mass (volume) of the microstructure.

In addition to tailoring the viscoelastic response of the composite, the current formulation allows for a general volume constraint setting, which we can use to impose constraints to a subset of the candidate materials, to sub-regions of the design domain, or to a combination of both. We solve the topology optimization statement using a new design variable update scheme that is tailored to solve this type of optimization problems in an efficient way.

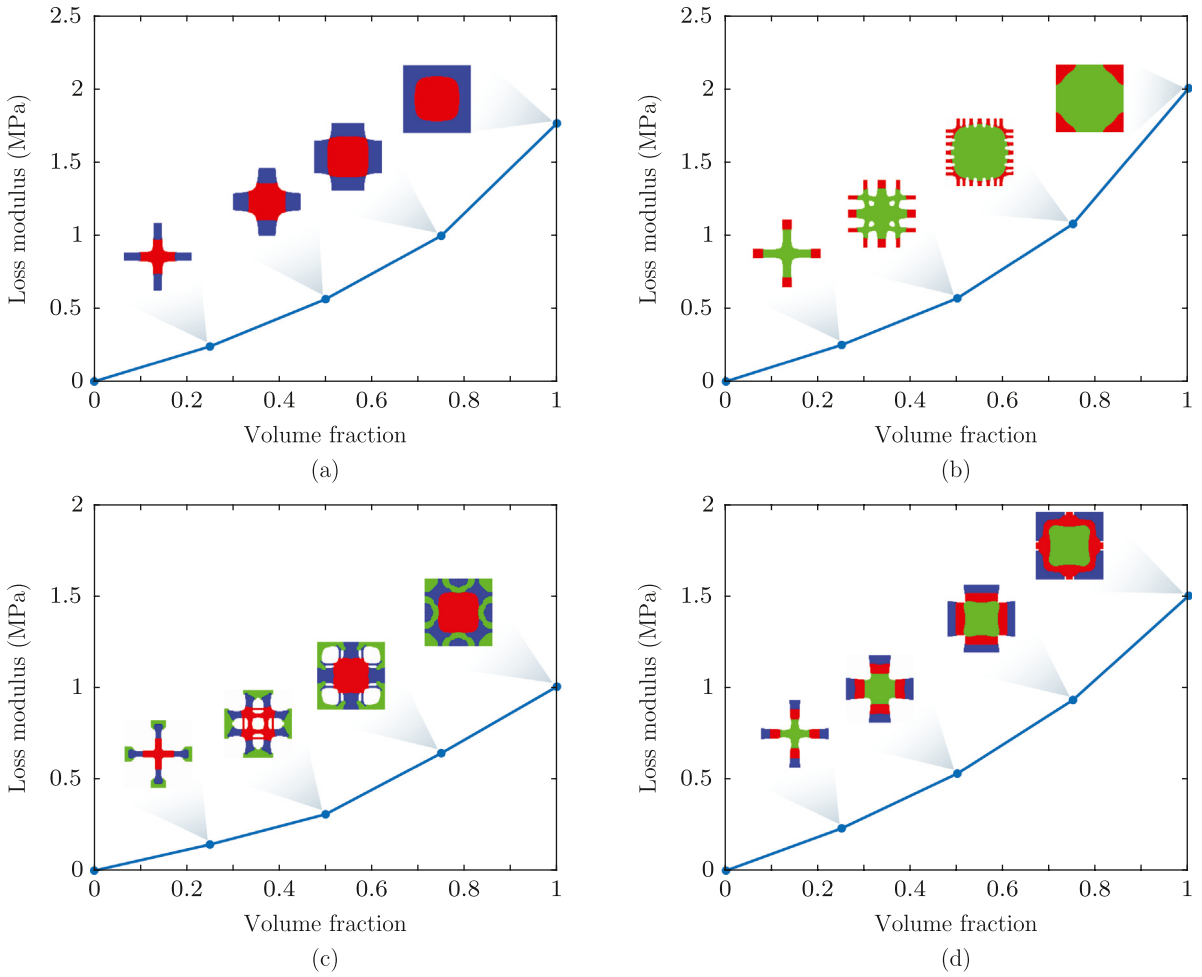

Fig. 11. Effect of the total volume fraction on the optimized loss modulus of the microstructure: The results in figures (a) and (b) correspond to volume constraint (41) and design frequencies of 0.1 Hz and 1 Hz, respectively. The results in figures (c) and (d) use volume constraint (42) and design frequencies of 0.1 Hz and 1 Hz, respectively.

The time to update the design variables using our approach is orders of magnitude smaller than that required by the widely used method of moving asymptotes.

As compared to designs of viscoelastic composites that are made of one or two materials, the framework presented in this study can be used to design composites made with an arbitrary number of candidate viscoelastic materials. This type of multi-phase viscoelastic composites can be engineered, for example, to have a wider operational frequency, so that they can damp energy efficiently for a wide range frequencies and/or temperatures. The results of this study show that we can design multi-phase viscoelastic composites to have a tailored loss modulus on a specified range of frequencies, which opens an avenue for the design of a new generation of architected viscoelastic materials.

Declaration of competing interest

The authors declare that they have no known competing financial interests or personal relationships that could have appeared to influence the work reported in this paper.

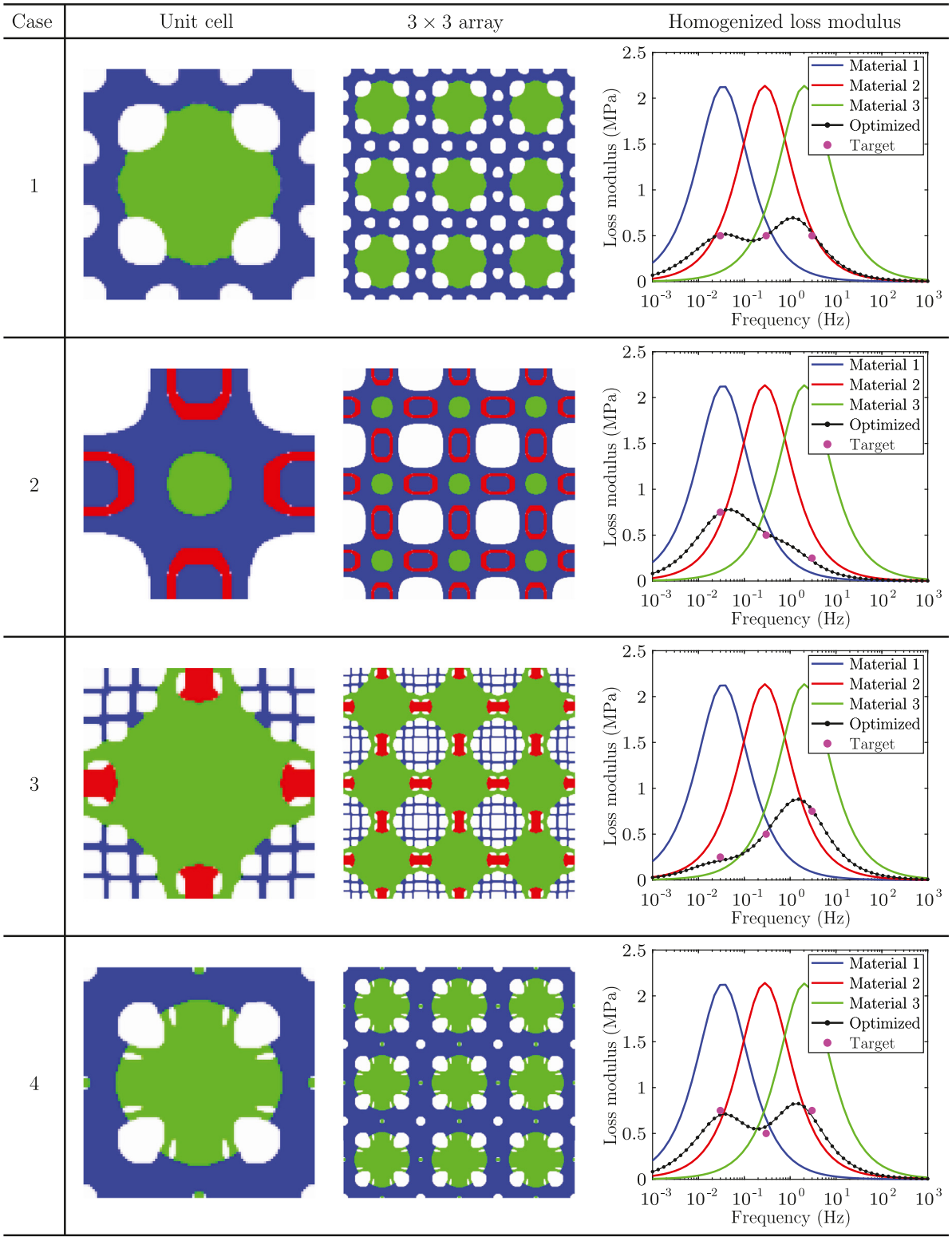

Fig. 12. Optimized 2D microstructures obtained for the target viscoelastic responses shown in Table 3.

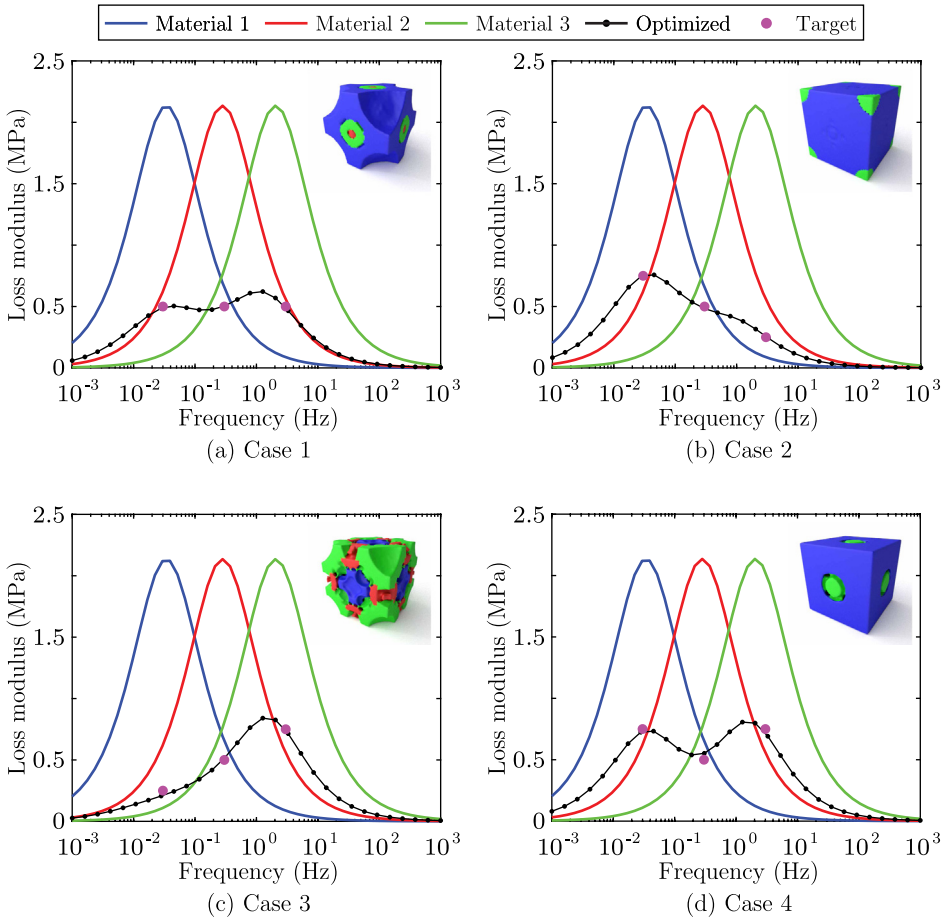

Fig. 13. Optimized 3D microstructures obtained for several different tailored viscoelastic responses.

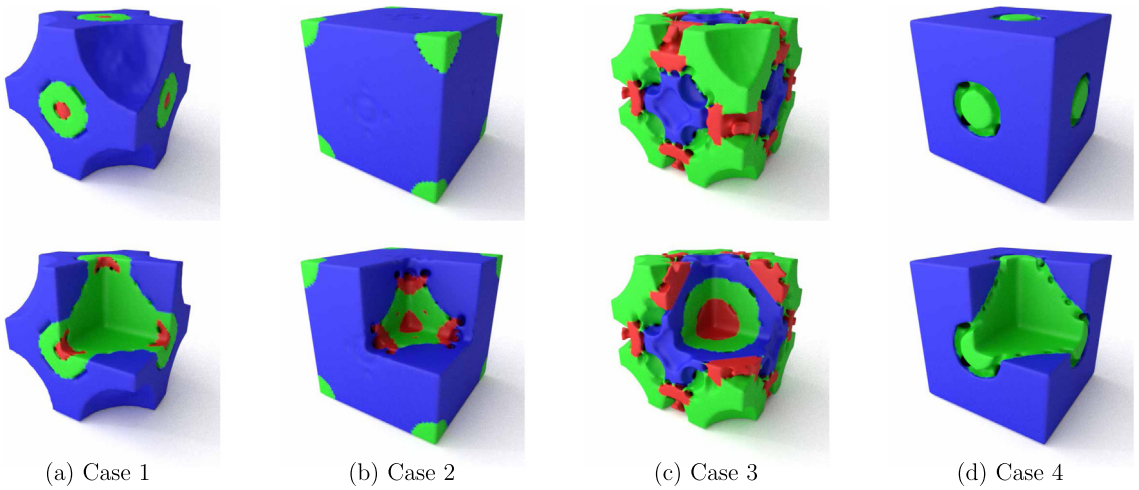

Fig. 14. Optimized 3D microstructures corresponding to the designs of Fig. 13. In the bottom row of figures, we have removed an octant of the geometry of each cell, which helps displaying the interior of each optimized microstructure.

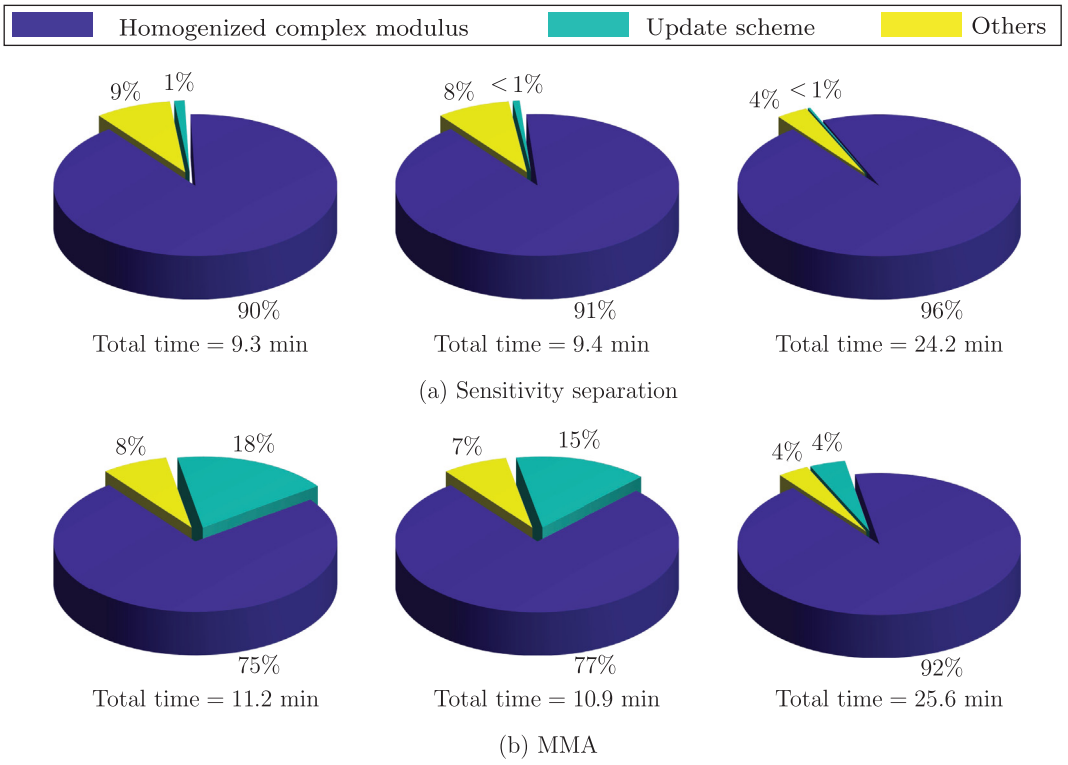

Fig. 15. Percentual breakdown of CPU time for the designs on the first row of Fig. 7 (left), Fig. 8 (middle), and Fig. 12 (right). The computational times are obtained using (a) the modified ZPR update scheme and (b) MMA.

Acknowledgments

We acknowledge the endowment provided by the Raymond Allen Jones Chair at the Georgia Institute of Technology. We thank Prof. Americo Cunha, from State University of Rio de Janeiro (UERJ), Brazil, for his insightful comments to the manuscript. The information provided in this paper as well as the interpretation of the results is solely that by the authors, and it does not necessarily reflect the views of the sponsors or sponsoring agencies.

Appendix. Verification

Before designing material microstructures, we verify the finite element implementation used to obtain the homogenized complex modulus tensor. To this end, we compare our numerical homogenization results with those obtained by Yi et al. [12] for two viscoelastic composites, each made of two materials. The two composites consist of a square unit cell with a circular inclusion. In the first composite, material 1 is used for the circular inclusion and material 2 is used for the matrix. In the second composite, the roles of the two materials are swapped. A 50% volume fraction for each material phase is used in both composites. The two composite materials are illustrated in Fig. 16. Yi et al. [12] simulated the viscoelastic material behavior for each phase based on a standard linear solid model, such that the stress relaxation function for the two material phases is as follows:

$$E_1(t) = 0.5 + 3e^{-t/10} \quad \text{and} \quad E_2(t) = 0.5 + 3e^{-t}. \tag{43}$$

Both material phases are assumed to have a Poisson's ratio $\nu = 0.35$.

In order to compare our results with those obtained by Yi et al. [12], we compute the homogenized loss tangent, $\tan\delta(\omega) = E''^H(\omega)/E'^H(\omega)$, where $E'^H(\omega)$ and $E''^H(\omega)$ are the homogenized storage and loss modulus of the composite, respectively. The homogenized loss tangent obtained from our implementation is compared against that

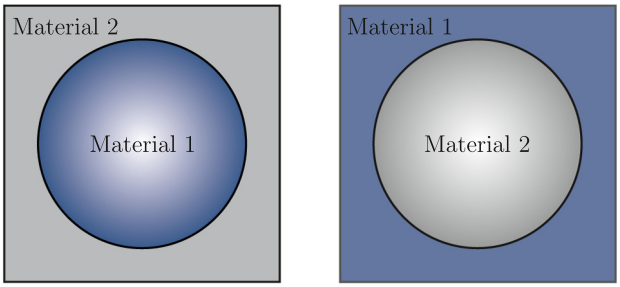

(a) Composite 1 (b) Composite 2

Fig. 16. A square unit cell with a circular inclusion is used to verify the finite element implementation that computes the homogenized complex modulus tensor. For composite 1 (left), material 1 is used for the circular inclusion and for composite 2 (right), material 2 is used for the circular inclusion.

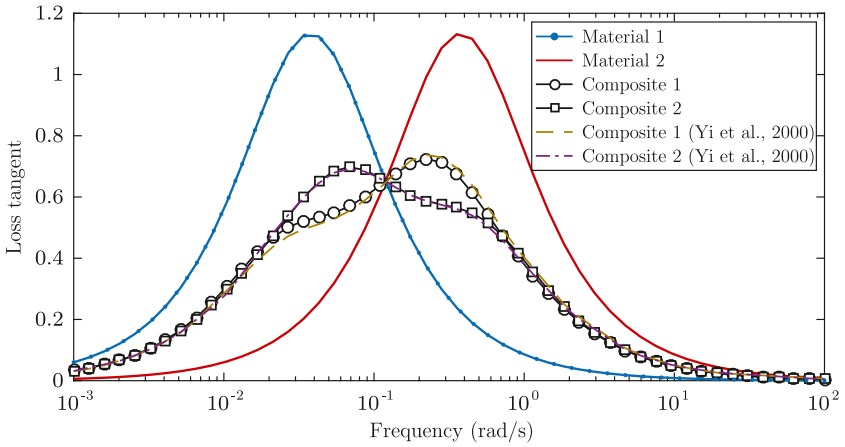

Fig. 17. Verification of the FE implementation used for the homogenization of viscoelastic materials. The homogenized loss tangent obtained from our numerical implementation agrees well with that obtained by Yi et al. [12] for the range of frequencies analyzed.

obtained by Yi et al. [12] for both composites, as depicted in Fig. 17. Only a slight difference between our results and those by Yi et al. [12] is observed, which may be due to differences in the finite element discretization, indicating a correct implementation of our finite element model.

Appendix B. Nomenclature

$\hat{v}$	Order of the Caputo fractional derivative
E''_e	Effective loss modulus for element e
E'_e	Effective storage modulus for element e
J	Objective function
N_c	Number of volume constraints
N_e	Number of elements in the FE mesh
R	Filter radius
$\bar{m}$	Total area (volume) of the microstructure normalized by its initial volume
$\bar{r}$	Sum of squared loss modulus residuals normalized by initial sum of squared residuals

$\bar{v}_j$ Volume fraction limit for constraint j

$\tilde{J}$ Non-monotonous convex approximation of the objective function

c Stiffness parameter for the fractional SLS model

g_j jth volume constraint

m Number of candidate materials

m_0 Initial area (volume) of the microstructure

p SIMP penalty coefficient

q Filter exponent

r_0 Initial sum of squared residuals

v_e Area (2D) or volume (3D) of element e in the FE mesh

$\mathcal{E}_j$ Set of element indices for constraint j

$\mathcal{M}_j$ Set of material indices for constraint j

$\partial J^+/\partial z_i^e$ **and** $\partial J^-/\partial z_i^e$ Positive and negative sensitivity components in sensitivity separation approach

${}_0D_t^{\hat{v}}(\cdot)$ Caputo fractional derivative of order $\hat{v}$

δ Mass penalization factor

γ Mixing penalty parameter

$\hat{\eta}$ Rigidity of the springpot

ξ Weight factor

$\mathbf{P}$ Filter matrix

$\mathbf{a}_i$, $\mathbf{b}_i$ Parameters used to define the convex approximation of the objective function

$\mathbf{h}$ Approximation of the diagonal of the Hessian matrix

$\mathbf{k}^*$ Complex stiffness matrix

$\mathbf{k}^R$ Real part of the complex stiffness matrix

$\mathbf{k}^i$ Imaginary part of the complex stiffness matrix

$\mathbf{u}_e^{A(ij)}$ Displacement vector of element e

$\mathbf{z}_1, \ldots, \mathbf{z}_m$ Vectors of design variables for candidate material, $i = 1, \ldots, m$

$\boldsymbol{\rho}_1, \ldots, \boldsymbol{\rho}_m$ Vectors of filtered densities for candidate material, $i = 1, \ldots, m$

$\tilde{\boldsymbol{\rho}}_1, \ldots, \tilde{\boldsymbol{\rho}}_m$ Vectors of element volume fractions for candidate material, $i = 1, \ldots, m$

References

[1] E.M. Kerwin Jr, Damping of flexural waves by a constrained viscoelastic layer, J. Acoust. Soc. Am. 31 (7) (1959) 952–962.

[2] C.D. Johnson, D.A. Kienholz, Finite element prediction of damping in structures with constrained viscoelastic layers, AIAA J. 20 (9) (1982) 1284–1290.

[3] M.D. Rao, Recent applications of viscoelastic damping for noise control in automobiles and commercial airplanes, J. Sound Vib. 262 (3) (2003) 457–474.

[4] H. Zheng, C. Cai, G.S.H. Pau, G.R. Liu, Minimizing vibration response of cylindrical shells through layout optimization of passive constrained layer damping treatments, J. Sound Vib. 279 (3–5) (2005) 739–756.

[5] M. Alvelid, Optimal position and shape of applied damping material, J. Sound Vib. 310 (4–5) (2008) 947–965.

[6] Z. Kang, X. Zhang, S. Jiang, G. Cheng, On topology optimization of damping layer in shell structures under harmonic excitations, Struct. Multidiscip. Optim. 46 (1) (2012) 51–67.

[7] S.Y. Kim, C.K. Mechefske, I.Y. Kim, Optimal damping layout in a shell structure using topology optimization, J. Sound Vib. 332 (12) (2013) 2873–2883.

[8] T. Yamamoto, T. Yamada, K. Izui, S. Nishiwaki, Topology optimization of free-layer damping material on a thin panel for maximizing modal loss factors expressed by only real eigenvalues, J. Sound Vib. 358 (2015) 84–96.

[9] R.A.S. Moreira, J. Dias Rodrigues, Partial constrained viscoelastic damping treatment of structures: A modal strain energy approach, Int. J. Struct. Stab. Dyn. 6 (3) (2006) 397–411.

[10] Z. Ling, X. Ronglu, W. Yi, A. El-Sabbagh, Topology optimization of constrained layer damping on plates using method of moving asymptote (MMA) approach, Shock Vib. 18 (1–2) (2011) 221–244.
[11] Y. Yi, S. Park, S. Youn, Asymptotic homogenization of viscoelasitc composites with periodic microstructures, Int. J. Solids Struct. 35 (17) (1998) 2039–2055.
[12] Y. Yi, S. Park, S. Youn, Design of microstructures of viscoelastic composites for optimal damping characteristics, Int. J. Solids Struct. 37 (35) (2000) 4791–4810.
[13] O. Sigmund, Materials with prescribed constitutive parameters: An inverse homogenization problem, Int. J. Solids Struct. 31 (17) (1994) 2313–2329.
[14] O. Sigmund, Tailoring materials with prescribed elastic properties, Mech. Mater. 20 (4) (1995) 351–368.
[15] E. Andreassen, J. Jensen, Topology optimization of periodic microstructures for enhanced dynamic properties of viscoelastic composite materials, Struct. Multidiscip. Optim. 49 (5) (2014) 695–705.
[16] C. Andreasen, E. Andreassen, J. Jensen, O. Sigmund, On the realization of the bulk modulus bounds for two-phase viscoelastic composites, J. Mech. Phys. Solids 63 (2014) 228–241.
[17] L.V. Gibiansky, R. Lakes, Bounds on the complex bulk modulus of a two-phase viscoelastic composite with arbitrary volume fractions of the components, Mech. Mater. 16 (1993) 317–331.
[18] L.V. Gibiansky, R. Lakes, Bounds on the complex bulk and shear moduli of a two-dimensional two-phase viscoelastic composite, Mech. Mater. 25 (1997) 79–95.
[19] W. Chen, S. Liu, Topology optimization of microstructures of viscoelastic damping materials for a prescribed shear modulus, Struct. Multidiscip. Optim. 50 (2) (2014) 287–296.
[20] X. Huang, S. Zhou, G. Sun, G. Li, Y. Xie, Topology optimization for microstructures of viscoelastic composite materials, Comput. Methods Appl. Mech. Engrg. 283 (2015) 503–516.
[21] E. Andreassen, J.S. Jensen, A practical multiscale approach for optimization of structural damping, Struct. Multidiscip. Optim. 53 (2) (2016) 215–224.
[22] W. Chen, S. Liu, Microstructural topology optimization of viscoelastic materials for maximum modal loss factor of macrostructures, Struct. Multidiscip. Optim. 53 (1) (2016) 1–14.
[23] A. Asadpoure, M. Tootkaboni, L. Valdevit, Topology optimization of multiphase architected materials for energy dissipation, Comput. Methods Appl. Mech. Engrg. 325 (2017) 314–329.
[24] O. Sigmund, S. Torquato, Design of materials with extreme thermal expansion using a three-phase topology optimization method, J. Mech. Phys. Solids 45 (6) (1997) 1037–1067.
[25] R.K. Patel, B. Bhattacharya, S. Basu, A finite element based investigation on obtaining high material damping over a large frequency range in viscoelastic composites, J. Sound Vib. 303 (3–5) (2007) 753–766.
[26] J. Stegmann, E. Lund, Discrete material optimization of general composite shell structures, Internat. J. Numer. Methods Engrg. 62 (14) (2005) 2009–2027.
[27] E. Lund, J. Stegmann, On structural optimization of composite shell structures using a discrete constitutive parametrization, Wind Energy 8 (2005) 109–124.
[28] E.D. Sanders, M.A. Aguiló, G.H. Paulino, Multi-material continuum topology optimization with arbitrary volume and mass constraints, Comput. Methods Appl. Mech. Engrg. 340 (2018) 798–823.
[29] X. Zhang, G.H. Paulino, A.S. Ramos Jr., Multi-material topology optimization with multiple volume constraints: a general approach applied to ground structures with material nonlinearity, Struct. Multidiscip. Optim. 57 (1) (2018) 161–182.
[30] T. Zegard, G.H. Paulino, Bridging topology optimization and additive manufacturing, Struct. Multidiscip. Optim. 53 (1) (2016) 175–192.
[31] B. Bourdin, Filters in topology optimization, Internat. J. Numer. Methods Engrg. 50 (9) (2001) 2143–2158.
[32] M.P. Bendsøe, Optimal shape design as a material distribution problem, Struct. Optim. 1 (1989) 193–202.
[33] M.P. Bendsøe, O. Sigmund, Material interpolation schemes in topology optimization, Arch. Appl. Mech. 69 (9–10) (1999) 635–654.
[34] E.D. Sanders, A. Pereira, M.A. Aguiló, G.H. Paulino, PolyMat: an efficient matlab code for multi-material topology optimization, Struct. Multidiscip. Optim. 58 (6) (2018) 2727–2759.
[35] K.V. Wong, A. Hernandez, A review of additive manufacturing, ISRN Mech. Eng. 2012 (2012) 1–10.
[36] M. Vaezi, H. Seitz, S. Yang, A review of 3d micro-additive manufacturing technologies, Int. J. Adv. Manuf. Technol. 67 (2013) 1721–1754.
[37] I. Gibson, D. Rosen, B. Stucker, Additive Manufacturing Technologies: 3D Printing, Rapid Prototyping, and Direct Digital Manufacturing, Vol. 2, Springer, 2015.
[38] D. Chen, X. Zheng, Multi-material additive manufacturing of metamaterials with giant, tailorable negative Poisson's ratios, Sci. Rep. 8 (1) (2018) 1–8.
[39] F. Mayer, S. Richter, J. Westhauser, E. Blasco, C. Barner-Kowollik, M. Wegener, Multimaterial 3D laser microprinting using an integrated microfluidic system, Sci. Adv. 5 (2) (2019) eaau9160.
[40] D. Han, C. Yang, N.X. Fang, H. Lee, Rapid multi-material 3D printing with projection micro-stereolithography using dynamic fluidic control, Addit. Manuf. 27 (2019) 606–615.
[41] X. Kuang, J. Wu, K. Chen, Z. Zhao, Z. Ding, F. Hu, D. Fang, H.J. Qi, Grayscale digital light processing 3D printing for highly functionally graded materials, Sci. Adv. 5 (5) (2019) eaav5790.
[42] M. Kapnistos, M. Lang, D. Vlassopoulos, W. Pyckhout-Hintzen, D. Richter, D. Cho, T. Chang, M. Rubinstein, Unexpected power-law stress relaxation of entangled ring polymers, Nature Mater. 7 (12) (2008) 997–1002.
[43] E. Kontou, S. Katsourinis, Application of a fractional model for simulation of the viscoelastic functions of polymers, J. Appl. Polym. Sci. 133 (23) (2016) 43505.

[44] F. Olard, H. Di Benedetto, General "2s2p1d" model and relation between the linear viscoelastic behaviours of bituminous binders and mixes, Road Mater. Pavement Des. 4 (2) (2003) 185–224.
[45] G.B. Davis, M. Kohandel, S. Sivaloganathan, G. Tenti, The constitutive properties of the brain paraenchyma: Part 2. fractional derivative approach, Med. Eng. Phys. 28 (5) (2006) 455–459.
[46] D. Craiem, F. Rojo, J. Atienza, R. Armentano, G. Guinea, Fractional-order viscoelasticity applied to describe uniaxial stress relaxation of human arteries, Phys. Med. Biol. 53 (17) (2008) 4543–4554.
[47] Z. Dai, Y. Peng, H. Mansy, R. Sandler, T. Royston, A model of lung parenchyma stress relaxation using fractional viscoelasticity, Med. Eng. Phys. 37 (8) (2015) 752–758.
[48] K.B. Oldham, J. Spanier, The Fractional Calculus: Theory and Aapplication of Differentiation and Integration to Arbitrary Order, in: Mathematics in Science and Engineering, vol. 111, Academic Press, INC., 1974.
[49] K.S. Miller, B. Ross, An Introduction to the Fractional Calculus and Fractional Differential Equations, first ed., Wiley-Interscience, 1993.
[50] M. D'Elia, M. Gulian, H. Olson, G.E. Karniadakis, A unified theory of fractional, nonlocal, and weighted nonlocal vector calculus, 2020, arXiv preprint arXiv:2005.07686.
[51] F. Mainardi, Fractional Calculus and Waves in Linear Viscoelasticity, Imperial College Press, 2010.
[52] G.W. Scott-Blair, The role of psychophysics in rheology, J. Colloid Sci. 2 (1) (1947) 21–32.
[53] O. Giraldo-Londoño, G.H. Paulino, W.G. Buttlar, Fractional calculus derivation of a rate-dependent PPR-based cohesive fracture model: theory, implementation, and numerical results, Int. J. Fract. 216 (1) (2019) 1–29.
[54] K. Singh, R. Saxena, S. Kumar, Caputo-based fractional derivative in fractional fourier transform domain, IEEE J. Emerg. Sel. Top. Circuits Syst. 3 (3) (2013) 330–337.
[55] R.S. Lakes, Viscoelastic Materials, Cambridge University Press, New York, NY, USA, 2009.
[56] M.P. Bendsøe, Optimization of Structural Topology, Shape, and Material, Vol. 414, Springer, 1995.
[57] A.A. Groenwold, L.F.P. Etman, On the equivalence of optimality criterion and sequential approximate optimization methods in the classical topology layout problem, Internat. J. Numer. Methods Engrg. 73 (3) (2008) 297–316.
[58] O. Giraldo-Londoño, L. Mirabella, L. Dalloro, G.H. Paulino, Multi-material thermomechanical topology optimization with applications to additive manufacturing: Design of main composite part and its support structure, Comput. Methods Appl. Mech. Engrg. 363 (2020) 112812.
[59] Y. Jiang, A.S. Ramos Jr., G.H. Paulino, Topology optimization with design-dependent loading: An adaptive sensitivity-separation design variable update scheme, Struct. Multidiscip. Optim. (2020) http://dx.doi.org/10.1007/s00158-019-02430-4, (in press).
[60] C. Fleury, CONLIN: An efficient dual optimizer based on convex approximation concepts, Struct. Optim. 1 (2) (1989) 81–89.
[61] C. Fleury, V. Braibant, Structural optimization: A new dual method using mixed variables, Internat. J. Numer. Methods Engrg. 23 (3) (1986) 409–428.
[62] K. Svanberg, The method of moving asymptotes—A new method for structural optimization, Internat. J. Numer. Methods Engrg. 24 (2) (1987) 359–373.
[63] M. Bruyneel, P. Duysinx, Note on topology optimization of continuum structures including self-weight, Struct. Multidiscip. Optim. 29 (4) (2005) 245–256.
[64] C.G. Broyden, The convergence of a class of double-rank minimization algorithms 1. general considerations, IMA J. Appl. Math. 6 (1) (1970) 76–90.
[65] R. Fletcher, A new approach to variable metric algorithms, Comput. J. 13 (3) (1970) 317–322.
[66] D. Goldfarb, A family of variable-metric methods derived by variational means, Math. Comp. 24 (109) (1970) 23–26.
[67] D.F. Shanno, Conditioning of quasi-Newton methods for function minimization, Math. Comp. 24 (111) (1970) 647–656.
[68] J.E. Dennis, R.B. Schnabel, Numerical Methods for Unconstrained Optimization and Nonlinear Equations, Vol. 16, SIAM, 1996.
[69] S.M. Marjugi, W.J. Leong, Diagonal hessian approximation for limited memory quasi-Newton via variational principle, J. Appl. Math. 2013 (2013) 1–8.
[70] L. Xia, P. Breitkopf, Design of materials using topology optimization and energy-based homogenization approach in matlab, Struct. Multidiscip. Optim. 52 (6) (2015) 1229–1241.